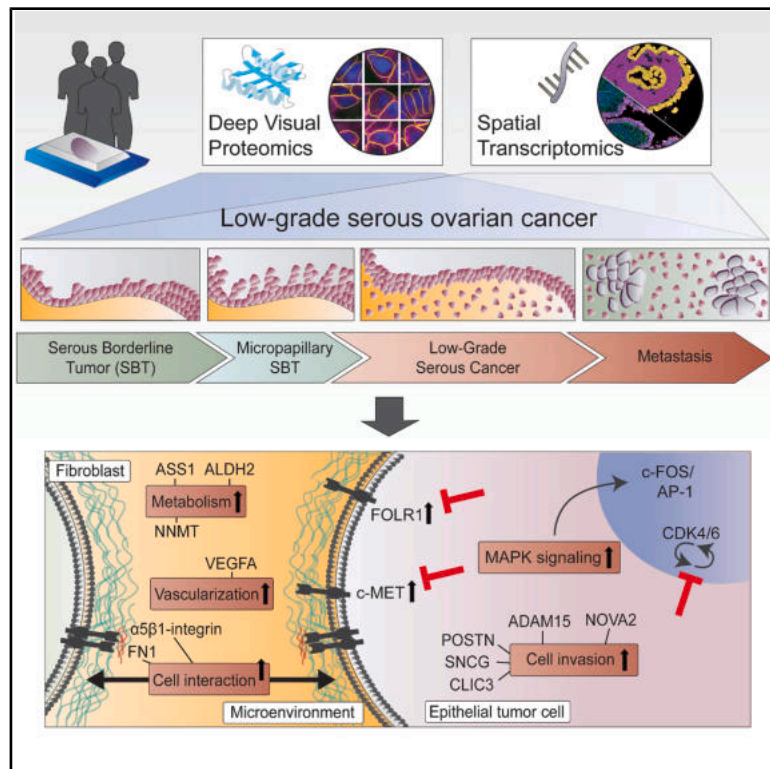


Cancer Cell

Spatial proteo-transcriptomic profiling reveals the molecular landscape of borderline ovarian tumors and their invasive progression

Graphical abstract



Authors

Lisa Schweizer, Hilary A. Kenny, Rahul Krishnan, ..., Ricardo R. Lastra, Matthias Mann, Ernst Lengyel

Correspondence

mmanm@biochem.mpg.de (M.M.), elengyel@uchicago.edu (E.L.)

In brief

Schweizer et al. profile the tumor progression from non-invasive serous borderline tumors of the ovary to metastatic low-grade serous ovarian cancer. By integrating cell-type resolved Deep Visual Proteomics and spatial transcriptomics, they identify and validate several drivers of transformation as well as a novel combination treatment for this chemo-resistant disease.

Highlights

- Integration of cell-type resolved spatial proteomics and transcriptomics
- Tumor progression from borderline ovarian tumors to metastatic low-grade serous cancer
- Micropapillary borderline tumors are an intermediate stage to low-grade ovarian cancer
- Mechanistic evidence supporting new combination treatments for low-grade ovarian cancer

Article

Spatial proteo-transcriptomic profiling reveals the molecular landscape of borderline ovarian tumors and their invasive progression

Lisa Schweizer,^{1,2} Hilary A. Kenny,² Rahul Krishnan,² Lucy Kelliher,² Agnes J. Bilecz,² Janna Heide,² Leonhard Donle,² Aasa Shimizu,² Andreas Metousis,¹ Rachele Mendoza,⁴ Thierry M. Nordmann,¹ Sarah Rauch,² Sabrina Richter,^{5,6} Yan Li,⁷ Florian A. Rosenberger,¹ Maximilian T. Strauss,³ Katherine C. Kurnit,² Marvin Thielert,¹ Edwin Rodriguez,¹ Johannes B. Müller-Reif,¹ S. Diane Yamada,² Fabian J. Theis,^{5,6} Andreas Mund,³ Ricardo R. Lastra,⁴ Matthias Mann,^{1,3,*} and Ernst Lengyel^{2,8,*}

¹Proteomics and Signal Transduction, Max Planck Institute of Biochemistry, 82152 Martinsried, Germany

²Department of Obstetrics and Gynecology/Section of Gynecologic Oncology, The University of Chicago, Chicago, IL 60637, USA

³Proteomics Program, Novo Nordisk Foundation Center for Protein Research, Faculty of Health and Medical Sciences, University of Copenhagen, 2200 Copenhagen, Denmark

⁴Department of Pathology, The University of Chicago, Chicago, IL 60637, USA

⁵Institute of Computational Biology, Computational Health Center, Helmholtz Munich, 85764 Neuherberg, Germany

⁶TUM School of Life Sciences Weihenstephan, Technical University of Munich, 85354 Freising, Germany

⁷Center for Research Informatics, The University of Chicago, 60637 Chicago, IL, USA

⁸Lead contact

*Correspondence: mmann@biochem.mpg.de (M.M.), elengyel@uchicago.edu (E.L.)

<https://doi.org/10.1016/j.ccell.2025.06.004>

SUMMARY

Epithelial serous borderline tumors (SBT) are non-invasive neoplastic ovarian lesions that may recur as chemo-resistant low-grade serous cancer (LGSC). While genetic alterations suggest a common origin, the transition from SBT to LGSC remains poorly understood. Here, we integrate cell-type resolved spatial proteomics and transcriptomics to elucidate the evolution from SBT to LGSC and its corresponding metastases in both stroma and tumor. The transition occurs within the epithelial compartment through an intermediary stage with micropapillary features, during which LGSC overexpresses c-Met and several brain-specific proteins. Within the tumor microenvironment, interconnectivity between cancer and stromal cells, along with enzymes degrading a packed extracellular matrix, suggests functional collaboration among various cell types. We functionally validated 16 drug targets identified through integrated spatial transcriptomics and proteomics. Combined treatment targeting CDK4/6 (miliciclib) and FOLR1 (mirvetuximab) achieved significant tumor reduction *in vivo*, representing a promising therapeutic strategy for LGSC.

INTRODUCTION

Serous ovarian tumors are the most common ovarian cancers. They are characterized either as high-grade (HGSC) or as a low-grade form (LGSC), the latter displaying only mild atypia and few mitotic features. Patients with LGSC tend to be younger (median age 45 years) than patients with HGSC (median age 62 years), and have slower growing, widely invasive tumors surrounded by dense fibrotic stroma and deep infiltration, making complete surgical removal challenging.^{1,2} If the tumor cannot be entirely removed at the time of the initial surgery, metastatic LGSC has an indolent clinical course with late recurrences and a low chance of cure. Although LGSC is a different disease entity, it is treated with the same standard platinum/taxane chemotherapy as HGSC. In LGSC, however, this treatment generally results in low clinical response rates and continued slow progression.³

LGSC has been understudied due to its low incidence (5–10% of all epithelial ovarian carcinomas⁴) and its unusual biology. Mutational profiling suggests that serous borderline tumors (SBTs) are precursor lesions of LGSC.⁵ Patients with SBT usually have an excellent prognosis after operative tumor removal, but 10–15% will recur with an LGSC.⁶ In contrast to HGSC, SBT and LGSC typically have wild-type p53, few DNA copy number changes, and a low rate of somatic mutations. Both SBT and LGSC have mutually exclusive mutations in *BRAF*, *KRAS*, or *ERBB2*,^{7–9} all upstream regulators of the mitogen-activated protein kinase (MAPK), known to drive cell proliferation. A role for the MAPK pathway and estrogen receptor signaling has been identified in SBT and LGSC; otherwise, little is known about their molecular landscapes. Histologically, the hypothetical transition from SBT to LGSC is characterized by irregularly contoured papillae with a hierarchical branching pattern that may progress in SBT to a micropapillary tissue architecture¹⁰ with mild

cytologic atypia. This phenotype, which remains non-invasive, signifies a higher risk of progression to LGSC.¹¹ Once cells evolve to LGSC, they diffusely invade the stroma and frequently metastasize to the omentum.¹²

Here, we set out to study the malignant transformation of SBT through putative intermediary steps to invasive and metastatic LGSC using spatial omics technologies and representative histologic cases from patients with SBT, micropapillary SBT (SBT-MP), and primary LGSC (LGSC-PT) and its corresponding metastases (LGSC-Met). We hypothesized that spatial omics technologies would be well suited to elucidating the underlying biology without bias. We recently developed Deep Visual Proteomics (DVP), which integrates high-content imaging, artificial intelligence (AI)-based cell recognition, laser microdissection, and mass spectrometry (MS) to preserve spatial information while quantifying the proteome in an unbiased manner.¹³ Hence, DVP is a powerful method for detecting compartment-resolved cell types using feature extraction from high-content images. We combined DVP with probe-based spatial transcriptomics to discover novel pathway alterations in LGSC and to find more effective treatments based on changes in protein and transcript expression during the transition from SBT to LGSC. The biological relevance of candidates identified by spatial omics was validated by IHC and targeted functional *in vitro* and *in vivo* screens, leading to new therapeutic strategies for LGSC treatment.

RESULTS

Spatial multi-omics of the transition from borderline tumor to low-grade serous cancer

Mutational profiling suggests a progression from SBT to SBT-MP and ultimately to LGSC, which may metastasize if not diagnosed and treated early¹⁴ (Figure 1A). We employed spatial proteomics (DVP)¹³ and transcriptomics (GeoMX) to analyze a discovery cohort consisting of four patients with SBT, four patients with SBT-MP, three cases of primary LGSC-PT, and patient-matched omental metastasis (LGSC-Met) (Table S1A) for compartment-resolved characterization of this progression (Figure 1B). For each patient, we studied the epithelial tumor and stromal compartment in a cell-type resolved manner in at least three different regions of interest (ROIs) per tissue section (Table S1B).

Deep Visual Proteomics (DVP) is the first method that enables compartment-resolved proteomic profiling of distinct cell types while preserving their spatial coordinates, allowing comparison with spatial transcriptomics. For DVP, we used markers for epithelial (EPCAM) and stromal cells (decorin) for immunofluorescent staining (Figure 1C). High-content images were imported into the Biology Image Analysis Software (BIAS), cell populations were segmented using the software integrated nucleiAIzer AI algorithm.¹⁵ Using a laser microdissection microscope, we collected approximately 200 cells (700 cell contours) at single-cell resolution into a 384-well plate for ultra-high sensitivity MS data acquisition.¹³ DVP detected and quantified a median of 5,456 different proteins in the epithelium and 3,919 in the stroma (Table S2A–C), with little inter- and intra-specimen variability and a high level of data completeness across all anatomic regions (Figures S1A–S1F). This represents substantial progress in

reducing the amount of sample needed to obtain reproducible, high-quality proteomics data at an unprecedented depth of thousands of proteins.^{13,16,17} A unique advantage of DVP is its ability to record and preserve the morphological characteristics of each cell within the tissue architecture. Borderline tumors exhibited larger epithelial cell size (Figure S1G) than LGSC, and the distance between epithelial cells increased in LGSC (Figure S1H).

Deep Visual Proteomics reveals the progression of borderline tumors to metastatic low-grade serous carcinoma

Principal Component Analysis (PCA) using data from spatial proteomics in the epithelial compartment stratified all four histologies (SBT, SBT-MP, LGSC-PT, and LGSC-Met). Micropapillary growth was an intermediary stage between noninvasive serous borderline and invasive LGSC (Figure 2A). Linear regression revealed 195 proteins with significant alterations in the invasive phenotypes (adj. *p*-value ≤ 0.05 , logFC >1.5 , Figures S2A and S2B; Table S2D). These gradual abundance changes included the adipogenesis regulatory factor ADIRF, which is associated with cisplatin resistance.¹⁸ These 195 proteins mark the transition from SBT to LGSC and its corresponding metastases.

SBTs with micropapillary features in the background of an SBT or uniform SBT-MP have a higher risk of recurrence as LGSC than conventional SBT.¹¹ However, whether SBT-MP (Figure 1A) is a precursor to LGSC remains controversial. The most significant changes between SBT and SBT-MP involved metabolic changes, particularly abundance changes in argininosuccinate synthase (ASS1), a key enzyme in the arginine biosynthetic pathway, along with ALDH6A1 and ALDH2 (Figure S3A). Several proteins changed markedly between SBT and SBT-MP, the first step in the hypothesized transition, but maintained their abundance in LGSC and its corresponding metastasis (Figures S2A and S2B; Figures S4A–S4D). Transcription factors AHDC1 and ERF, along with stemness-associated proteins AQP5 and ASB6, were upregulated in SBT-MP, but remained stable in LGSC and its metastases (Figures S4A and S4B). The tumor suppressor CDKN2A¹⁹ was downregulated in SBT-MP and remained low in LGSC and LGSC-Met (Figure S4C). While SBT-MP proteomic profiles were more similar to SBT than to LGSC, they visually displayed hallmarks of malignant transformation, such as micropapillary tissue architecture, consistent with co-localization of SBT/SBT-MP in the PCA (Figure 2A). One patient with both SBT-MP and LGSC on a single slide confirmed TRIM25 downregulation in LGSC (Figure S5).

A comparison of SBT and LGSC-PT in the epithelial compartment identified 963 differentially expressed proteins (Table S2E). Upregulated proteins included SHMT1 and TAGLN, which were previously linked to HGSOE (Figure 2B). LGSC and its metastases showed progressive loss of ZMYND10 and OSCP1/NOR1, two tumor suppressors involved in epigenetic regulation,^{20,21} along with Anterior Gradient Protein 2/3 (AGR2/3), which was previously implicated in the progression of SBT to LGSC²² (Figure S2B).

The MAPK signaling pathway is altered in over 50% of LGSC and 60% of SBTs.²³ LGSC showed enrichment of several members of the oncogenic MAPK pathway compared to borderline tumors (Figures 2C, S3B, and S3C; Table S2F).^{2,23} KRAS,

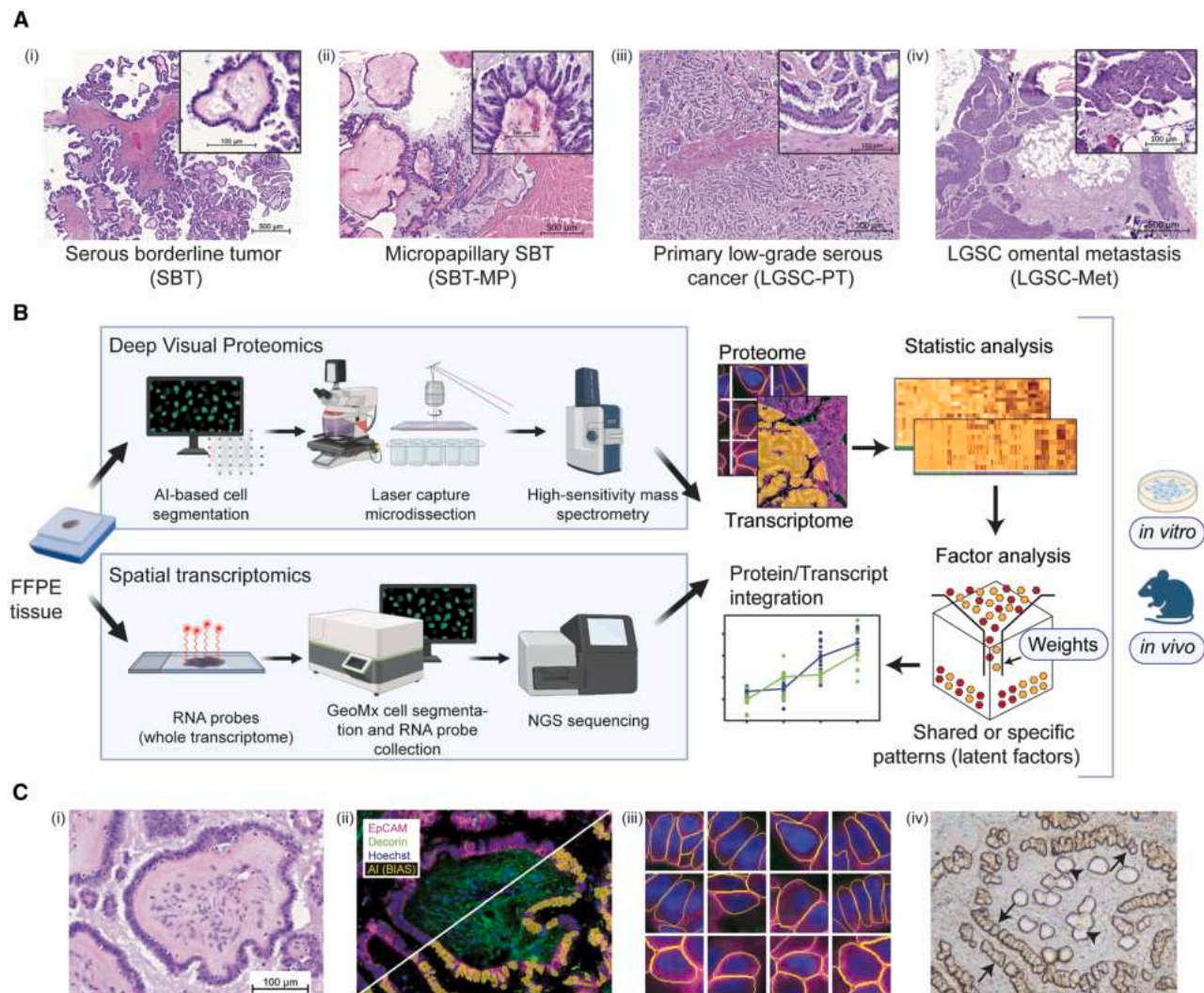


Figure 1. Characterization of serous borderline and low-grade ovarian cancer

(A) Representative H&E images of the putative transformation sequence from (i) serous borderline tumor (SBT, non-invasive) via (ii) micropapillary lesions (SBT-MP) to (iii) low-grade serous cancer-primary tumor (LGSC-PT), and (iv) metastasis (LGSC-Met). The papillary architecture with a hierarchical branching pattern is characteristic of SBT. Scale bars low magnification: 500 μ m; high magnification: 100 μ m.

(B) Experimental workflow combining bioinformatics and multi-omics integration (MOFA+) to identify potential therapeutic targets and validate them functionally. Results from a discovery cohort were confirmed in an independent cohort using IHC.

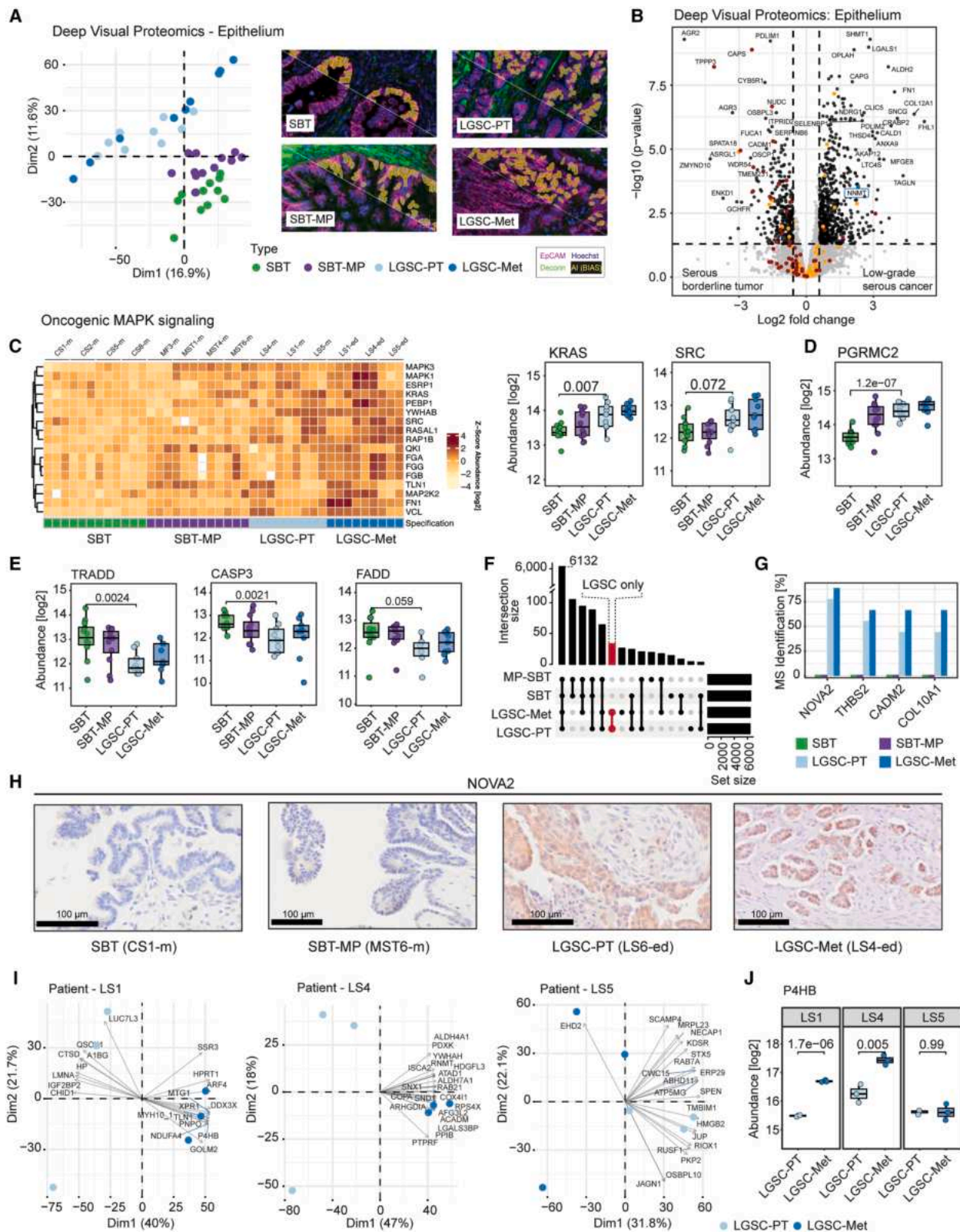
(C) AI-based cell recognition and laser-based dissection in DVP. (i) H&E of an SBT. (ii, iii) Immunofluorescence outlining cell contours. Staining for malignant epithelial cells (EpCAM, purple) and stromal (decornin, green) as well as artificial intelligence (AI)-based recognition of tumor cells (yellow – below diagonal line) using the BIAS software. (iii) Morphology of single epithelial cells as recognized by artificial intelligence. (iv) Brightfield image of the same sample in i and ii showing the tissue after single-cell extraction. Gaps indicate microdissected epithelial (arrows, EP) and stromal cells (arrowheads, ST) while the surrounding tissue is intact. Scale bar: 100 μ m.

Also see [Table S1](#).

SRC, MAPK3 (ERK1), MAP2K2 (MEK2), and the transcriptional repressor ERF gradually increased from SBT to LGSC (Figures 2C and S3C). While KRAS and BRAF mutations were present in some cases, they were not universal (Table S1C). TGF- β pathway components, including oncogenic ADAM17, were upregulated in SBT-MP and LGSC, promoting EMT²⁴ and T cell suppression²⁵ (Figure S3D). Most SBT and LGSC tumors expressed estrogen and progesterone receptors (Table S1D), with PGRMC2 increasing from SBT to SBT-MP, suggesting a role for progesterone in early LGSC transition (Figure 2D).²⁶

SBT expressed PAX8, a marker of fallopian tube secretory cells,¹⁹ along with ciliated cell proteins (CAPS, TPPP3, and NUDC), which were lost upon progression to LGSC (Figure S3B, S3E; Table S2F). In LGSC, immunofluorescence confirmed that ciliated cells were sparse (Figure S3F) and associated with reduced expression of apoptotic proteins, including FADD, CASP-3/8, and TRADD (Figure 2E).

Among proteins identified by MS in LGSC and metastasis but absent in SBT and SBT-MP, we found exclusive expression of the splicing regulator NOVA2, which is generally expressed in



(legend on next page)

the brain but not in the healthy ovary²⁷ (Figures 2F and 2G; Table S2G). NOVA2 was detected in the medium abundance range of MS intensities in the LGSC-PT group but was completely absent in borderline tumors (Figure S3G). We confirmed NOVA2 expression by IHC (Figures 2H; Table S3A; Figure S6A,E), noting that its differential expression was only evident at the proteome level and not the transcriptome level. When comparing SBT and LGSC-PT, 14.5% of all proteins showed significantly different abundances, in contrast to only 0.3% between LGSC-PT and LGST-Met (Figure S3A). This included metastatic upregulation of neudesin (NENF), a protein that regulates the proliferation of neural progenitor cells.²⁸ Analysis of individual patients revealed significant proteomic heterogeneity between metastases and LGSC, with 6.2% (414 proteins, LS4-m), 3.7% (247 proteins, LS1-m), and no differential expression in LS5-m across patients (Table S2H). Each patient displayed a specific set of proteins contributing to the stratification between LGSC-PT and metastasis (Figure 2I). These changes included the disulfide-isomerase P4HB, which is associated with glioma progression in the brain²⁹ (Figure 2J).

Analysis of the tumor microenvironment using spatial proteomics

Deep Visual Proteomics enables protein detection in different tissue compartments through AI-based recognition of individual cell types. Analysis of decorin+ stromal cells (Figure 3A), revealed 178 proteins with significant changes during the transition from SBT to LGSC (Figure S7; Table S2D). Principal component analysis showed distinct protein expression patterns in SBT and SBT-MP compared to LGSC and its metastasis (Figure 3B), highlighting major stromal changes during tumor invasion (Figure S8A; Table S2I). Unlike the epithelial compartment (Figure 2A), where SBT-MP exhibited intermediate traits, stromal profiles of SBT and SBT-MP remained similar, suggesting that early SBT-MP changes originate in epithelial cells. The most pronounced stromal protein expression occurred during the transition from SBT to LGSC (629 differentially expressed proteins), including the upregulation of ANXA2 and its regulator

S100A10, which play central roles in cancer cell proliferation and invasion³¹ (Figure 3C). The dominant biological processes upregulated in LGSC-PT involved cytoskeletal dynamics; we found an upregulation of actin (ACTG1) and its central regulator ROCK2,³² alongside other components of cytoskeletal organization (ARPC2-4, CFL1, ITSN1, and PAK1/2), all linked to ephrin signaling (Figure S8B; Table S2F).

We found an increased abundance of cell-cell adhesion proteins in invasive LGSC, including the suppressors of apoptosis COMP and GAS6, consistent with decreased apoptosis in the epithelium (Figures 2E and S8C). Further analysis of interaction partners revealed more ligands and receptors upregulated in LGSC-PT than SBT (Figures 3D, S8D, and S8E)³⁰ such as the interaction between epithelial MMP14 and its stromal receptor SDC1, a known driver of invasion.³³ The $\alpha 5 \beta 1$ -integrin (ITGA5, ITGB1) receptors on stromal cells and their ligand fibronectin (FN1), which was abundant in both cell types, increased during progression to LGSC-PT (Figure 3E), and the metastatic epithelial cells (Figure S4E). Using IHC, we validated the expression of $\beta 1$ -integrin and fibronectin in both discovery and validation cohorts (Figures 3F, S6C, S6D, S8F, and S8G; Table S3A).

Analysis of cell-type specific interactions showed that stromal-stromal interactions were primarily mediated by integrins (ITGA5, ITGAV, and ITGA11) and thombospondins (THBS3 and THBS2) (Figure S8D). In epithelial-epithelial interactions, we identified the metalloproteinase ADAM17 interacting with APP and ICAM1, and the neuronal protein PRNP (CD230) interacting with laminins (LAMC1, LAMA3, and LAMB3) (Figure S8E). Both MMP2 and its regulator TIMP3 showed upregulation in the tumor microenvironment during progression (Figure 3G).³⁴ Supporting this finding, we identified CD147 (BSG), which promotes MMP vesicle secretion from tumor cells and showed upregulation in the epithelial compartment as early as SBT-MP³⁵ (Figure 3H).

The stromal transition from non-invasive to invasive tumor stages was characterized by increased glucose metabolism, including the upregulation of the rate-limiting gluconeogenic enzymes FBP1 and PCK2/PEPCK³⁶ (Figure 3I). NNMT, a metabolic regulator of fibroblasts that we previously showed to control the

Figure 2. Deep Visual Proteomics on the epithelial tumor compartment confirms known and identifies novel pathways in the transition of SBT to LGSC

(A) Principal Component Analysis (PCA) of the epithelium separates serous borderline tumors, serous borderline tumors with a micropapillary pattern, invasive low-grade serous cancer, and corresponding metastasis. This transition is evident in the diagonal of PC1 and PC2 from the lower right to upper left. AI-based recognition of epithelial cells using immunofluorescence (EpCAM-purple, decorin-green) below the white diagonal line, followed by AI segmentation (yellow). Scale bar: 10 μ m.

(B) Volcano plot of the differential epithelial protein expression between SBT and LGSC-PT. Proteins matching the significance for differential regulation criteria are highlighted in black, markers of secretory cells in orange and ciliated cells in red. NNMT, an important target in the stromal analysis, is highlighted in blue.

(C) Proteins of the mitogen-activated protein kinase (MAPK) signaling pathway show a gradual increase toward LGSC and corresponding metastasis (heatmap). Commonly altered Ras and Ras-regulating proteins (boxplots). Paired samples are highlighted by the patient identifier (e.g., LS1-m and LS-ed, see also Table S1).

(D) Boxplots of significantly changed membrane-associated progesterone receptor component 2 (PGRMC2) between the four groups.

(E) Apoptosis-related proteins show reduced abundance from SBT to LGSC-Met.

(F) Upset plot comparing group-specific protein detection patterns. The plot shows proteins detected exclusively in certain histological groups by mass spectrometry (not shown in 2B,S3A). The set size represents total proteins per group; the intersection size indicates proteins shared between specific groups.

(G) Protein subset from (F), LGSC only. Bars present the percentage of samples in which mass spectrometry identified the four most frequent proteins per group.

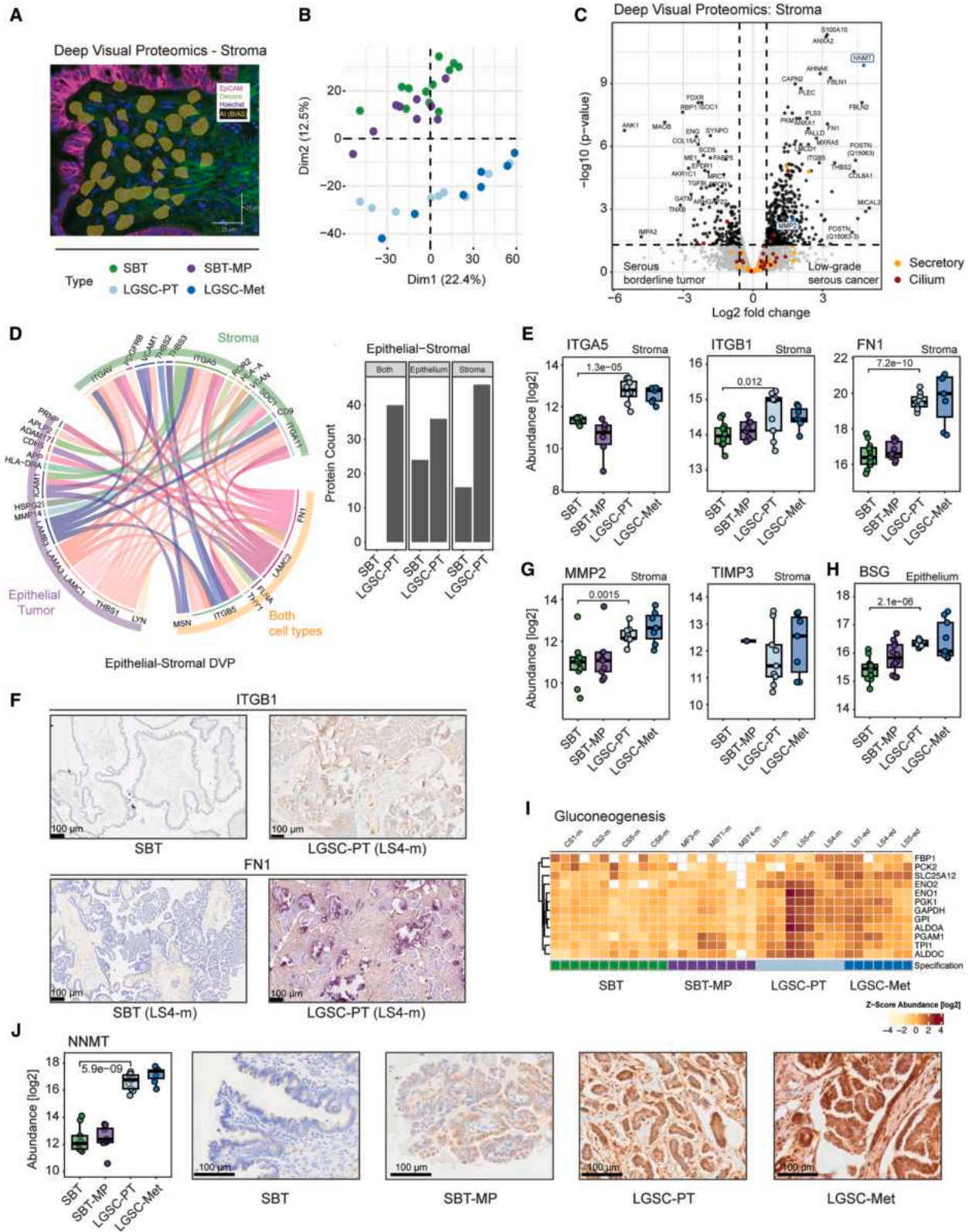
(H) Immunohistochemistry for NOVA2. Scale bars: 100 μ m.

(I) PCA of individual patients with invasive tumors stratifying LGSC and corresponding metastases. Major protein contributors are highlighted by arrows (indicating the direction of contribution).

(J) P4HB protein expression showing significant alteration in two out of three patients.

Boxplots show the 25- and 75-percentile and the median value as center line. Whiskers span the 1.5-fold interquartile range, and each data point represents a patient-derived sample. The significance between comparisons was determined using a two-sided Student's *t* test.

Also see Figures S1–S6 and Tables S1 and S2.



(legend on next page)

transition from normal fibroblasts to cancer-associated fibroblasts (CAFs),³⁷ was among the most highly upregulated proteins in invasive LGSC stroma and epithelium (Figures 3J and 2B).

Spatio-transcriptomics analysis of the progression of serous borderline tumor to invasive low-grade serous carcinoma

We performed spatial transcriptomics using the GeoMx technology on serial sections from the four histologies previously analyzed by spatial proteomics (Figures 1A and 1B). This “Nanostring” method involved hybridization with over 18,000 RNA probes, followed by focused UV light exposure to selectively release probe barcodes from cell types of interest for NGS analysis (Tables S4A and S4B). The sequencing data generally indicated high saturation (9,872 targets detected after QC, Figure S9). To align the spatial transcriptome with the proteome, we employed immunofluorescence staining using compartment-specific antibodies to match corresponding ROIs (Figure 4A).

A total of 1,386 transcripts in the epithelium were differentially expressed between SBT and LGSC-PT (Table S4C). SBT showed upregulation of mucin-regulating AGR2 and the gel-forming mucin MUC5B (Figure 4B). At the same time, LGSC-PT had higher levels of the CA-125 binding partner mesothelin (MSLN) and the serine protease KLK6, an MAPK-regulated protein linked to ovarian tumor recurrence.³⁸ Several nervous system-associated transcripts, such as SPOCK2 and γ -synuclein (SNCG) were also upregulated in LGSC-PT (Figure 4B).

During SBT-to-LGSC progression, SBT-MP exhibited early upregulation of MAPK-regulated transcription factor MAZ and oocyte development-associated DUX4³⁹ (Figure S10A). Additional early changes included increased expression of JUNB, FOS, and FOSL2, which rose from SBT to SBT-MP, remained high in invasive tumors, and has been linked to chemoresistance in HGSC⁴⁰ (Figures 4C and S11A), consistent with their upstream regulators EGFR and SHC1 (Figures S10B and S10C). In contrast, invasive cancer showed downregulation of progesterone-associated endometrial protein (PAEP) and the p53-stabilizing transcriptional repressor HIC1 compared to SBT (Figure S11B; Tables S4C and S4D).

GSEA pathway analysis revealed changes in mucins such as MUC3A, MUC5B, and MUC16 (CA-125) along with alterations in tissue migration, semaphorin signaling, and c-MET associated signaling (Figures 4D, S10D, and S10E; Table S4E). The c-Met receptor tyrosine kinase showed significant upregulation in LGSC and metastases at the transcript level, which we confirmed by IHC (Figures 4E, 4F, and S6G). Related upregulated transcripts involved in c-MET signaling included pathway regulators (HGS, ARF6, and RAB4A) and signaling elements (SHC1, PTPN11, and PTK2). Supporting the spatial proteomics data, we also found changes in regulatory components of CDK signaling, including upregulation of the G1/S-specific cyclin-D1 (CCND1) in LGSC-PT and downregulation of the G1/S transition regulator and tumor suppressor, RB1 (Figure S10F).

A PCA revealed differences between SBT and SBT-MP in the epithelium, while stromal gene expression distinguished SBT/SBT-MP from LGSC-PT/LGSC-Met (Figures 4G, S12A, and S12B). Several stromal transcripts showing upregulation between SBT and LGSC, such as S100A10, C3, and NNMT (Figure 4H; Table S4F), matched those identified by spatial proteomics, providing cross-confirmation between the two modalities (Figure 3C). We also identified changes in genes detected only as transcripts, such as the metalloproteinase, ADAM15, and factors involved in oxygen-homeostasis (e.g., VEGFA and HIF1 α), which increased during the transition from SBT to SBT-MP (Figure 4I). Interestingly, the stem cell markers LGR5 and FOXL2 showed high abundance in SBT but steadily decreased as tumors transformed and metastasized (Figures S11C, S11D, and S12A). Additionally, the neural axon guidance factor SLIT2 was highly expressed in LGSC-Met, while the cell-adhesion protein CDHR1 was downregulated (Figure S12A). Genes upregulated solely on the RNA level in CAFs⁴¹ included those involved in angiogenesis and hypoxia (Figures 4J and S12C).

Integration of multi-modal spatial data reveals complex molecular patterns

We integrated single cell type proteomics, transcriptomics, and H&E staining to understand the tumor organ (Figure 5A) comprehensively. We found 67.7% of proteins and 32.7% of transcripts

Figure 3. Deep Visual Proteomics of the stromal compartment uncovers a bimodality in the transition of SBT to LGST

- (A) Immunofluorescence outlining the extraction of cell equivalents from the stroma (EpCAM-purple, decorin-green, AI-segmentation - yellow). Scale bar: 25 μ m.
- (B) PCA comparing stromal protein expression shows the separation of serous borderline and micropapillary tumors from invasive low-grade serous cancer and corresponding metastases. The stratification was most evident in dimension 2 (12.5%).
- (C) Volcano plot of differential stromal protein expression between SBT and LGSC-PT in the stromal compartment. A fold change cutoff of 1.5 and a q-value cutoff of 0.05 are indicated by vertical and horizontal lines, respectively. Proteins matching the significance for differential regulation criteria (black), markers of secretory cells (orange), and ciliated cells (red), MMP2 and NNMT (blue). For the protein POSTN, the main protein (UniProt ID Q15063) and its isoform Q15063-3 are annotated.
- (D) Chord diagram (left) representing the potential interactions between cell-cell adhesion ligands and receptors that are significantly upregulated in LGSC compared to SBT; interactions between epithelial and stromal cells (*Omnipath* database³⁰). Plots depict binary interaction partners by extrapolating quantitative information on protein interactions. Quantitative information (right): total count of potentially interacting proteins between cell types.
- (E) Protein abundances for α 5-integrin (ITGA5), β 1-integrin (ITGB1), and fibronectin (FN1).
- (F) Immunohistochemistry of ITGB1 and FN1 in SBT and LGSC-PT, respectively.
- (G) Stromal cell protein abundance for MMP2 and its regulator TIMP3.
- (H) Epithelial cell protein abundance for the inducer of MMP release, CD147 (BSG).
- (I) Proteins involved in gluconeogenesis increase toward LGSC and corresponding metastasis.
- (J) NNMT protein abundance and immunohistochemistry.

Boxplots show the 25- and 75-percentile and the median value as the center line. Whiskers span the 1.5-fold interquartile range, and each data point represents a patient-derived sample. The significance between comparisons was determined using a two-sided Student's *t* test. Paired samples are labeled with the patient identifier (e.g., LS1-m and LS1-ed). Scale bars: 100 μ m.

Also see Figures S6–S8 and Tables S2 and S3.

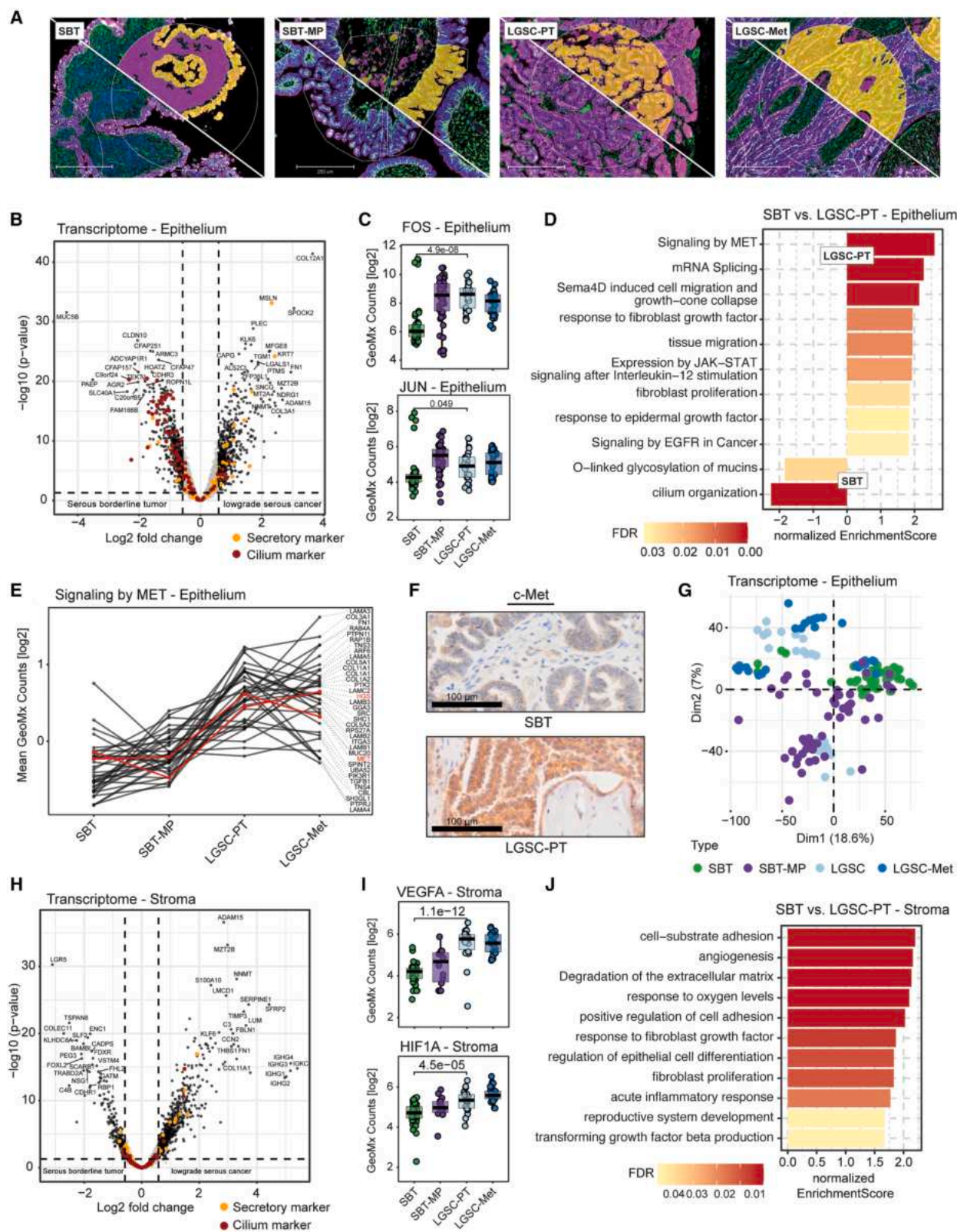


Figure 4. Spatial transcriptomics of SBT and LGSC

(A) Immunofluorescence for pan-cytokeratin (purple), decorin (green), and nuclei (blue) for exemplary regions. Tumor and stroma compartments are shown above the white diagonal line in yellow and magenta, respectively. Regions of interest are outlined with fine white lines. Scale bars: 250 μm .

(legend continued on next page)

overlapping between DVP and Nanostring in the stroma, compared to 67.9% of proteins and 44.5% of transcripts in the epithelium (Figure S13A). The overlap was lower for differentially expressed proteins and transcripts, with 30.9% of proteins and 18.9% of transcripts overlapping in the stroma and 20.7% of proteins and 14.2% of transcripts in the epithelium. Many genes were only detected as transcripts in the Nanostring data and many only as proteins in the DVP data (Figure S13B; Tables S2E, S2I, S4C, and S4F). Both technologies showed adequate cell type stratification, with better separation by DVP compared to GeoMx (PCA variance: DVP - 28.2%; GeoMx - 8.3%, Figure S13C), and clear enrichment of cell-type-specific markers (Figure S13D).

Analysis of the proteome and transcriptome datasets across the four histologies revealed a positive correlation for 1,142 out of 4,992 genes in the epithelium across the transition from SBT to LGSC-Met (Figure 5B). In the stroma, only 84 of 3,746 genes significantly correlated between transcripts and proteins (Figure 5C). Only 32 genes were anti-correlated between the two technologies in the epithelial compartment, including ABT1, ZMIZ1, and CIR1, and only CHST14 in the stroma. Folate-receptor α (FOLR1) showed concordant epithelial expression levels across both datasets and in IHC (Figures S6B and S6F; Table S3B). FOLR1 is a target for mirvetuximab soravtansine, an FDA-approved treatment for platinum-resistant high-grade serous cancers,⁴² but is not currently used for LGSC (Figure 5D). Additionally, we observed increased FOLR1 expression in LGSC-Met compared to epithelial LGSC-PT (Figure S4E). The cyclin-dependent kinase CDK4 showed upregulation in both datasets, while the CDK-inhibitor CDKN2A was consistently downregulated (Figures 5E and 5F). CDK6 was upregulated at the proteomic but not the transcriptomic level (Figure 5G).

To identify markers of tumorigenesis, we used the Multi-Omics Factor Analysis (MOFA+)⁴³ framework to integrate our datasets. MOFA+ identifies latent factors and underlying axes of variation in the data that summarize the main sources of variation across datasets. The integration supported SBT-MP as a transitional stage and revealed the heterogeneous stroma of LGSC-PT (Figures 5H and 5I). Based on the MOFA+ analysis scores, we generated a target panel of markers associated with tumorigenesis. We selected the ten highest-scored proteins and transcripts with significant up- or downregulation, separately for epithelial or stromal cells (Figure S13E; Table S3C). Both

technologies identified most of these as potential biological drivers (e.g., SNCG in the epithelium and NNMT, POSTN, and ADAM15 in the stroma).

Importantly, we used CIBERSORTx, based on our recently published single-cell RNA sequencing atlas of the postmenopausal ovary,^{44,45} to deconvolute the decrin+ stroma and found minimal immune and endothelial cell contamination (Figure S13F).

Testing drug targets in low-grade serous cancer *in vitro* and *in vivo*

Having characterized the proteomic and transcriptomic landscape of progression to metastatic LGSC, we investigated the functional significance of the potential drivers in the transition between SBT and LGSC. LGSC cell lines were characterized by MS-based proteomics, revealing a positive correlation with the proteomic profiles of both SBT and LGSC-PT epithelium. The highest correlations were observed between VOA6406 and SBT, and VOA4627 and LGSC-PT (Figure 6A). Proteomics and transcriptomics data integration led to target selection for a siRNA screen. Knock-down of ADAM15, CLIC3, POSTN, SNCG, and NOVA2 significantly inhibited VOA4627 migration (Figure 6B). The individual knock-down of these genes inhibited the proliferation of VOA4627 and invasion of VOA4627 and VOA6406 cells. The knock-down of NOVA2 and SNCG significantly inhibited proliferation in VOA6406, which is phenotypically closer to SBT than VOA4627 (Figures 6C, 6D, S14A–S14D).

NOVA2 was absent in SBT and SBT-MP but present in invasive tumors (Figures 2F–2H). The knockdown of NOVA2 followed by MS-based proteomics revealed decreased expression of 25 proteins, including the methyltransferase DNMT1, the epigenetic regulator UHRF1, and the Cyclin-dependent kinase CDK1 (Figure 6E). Importantly, we identified a correlation between c-MET and NOVA2 levels, suggesting potential regulation linked to the exclusive expression of NOVA2 in invasive tumors. NNMT was among the most upregulated stromal drivers in LGSC (Figures 3C and 3J). Knock-down of NNMT in immortalized human CAFs³⁷ inhibited both the CAF-conditioned media-driven proliferation and invasion of VOA4627 and VOA6406 cells (Figures 6F, 6G, S14E, S14F).

We next investigated the effect of inhibiting the prominent pathways and targets identified through our molecular analyses (Figures 2, 3, and 4) and our integrative omics approach

(B) Differential transcript analysis of the epithelial compartment comparing borderline and low-grade serous cancer (Volcano plot). Markers for ciliated (red) and secretory cells (orange) are highlighted.

(C) GeoMx counts for JUN and FOS across the progression series.

(D) GSEA biological pathway enrichment analysis based on the spatial transcript results comparing SBT and LGSC-PT in the epithelial compartment (Pathway REACTOME, Gene Ontology Biological Processes) on the comparison in (B).

(E) Profile plot of pathway-associated proteins determined in (D) for 'Signaling by MET'. Proteins with critical roles in the pathway (MET, HGS) are annotated in red.

(F) IHC of c-MET in SBT and LGSC-PT. Scale bars: 100 μ m.

(G) Nanostring PCA using transcripts in the epithelium for the indicated histologies.

(H) Stroma. Differential transcript abundance of SBT versus LGSC-PT. Protein markers for ciliated and secretory cells are highlighted in red and orange, respectively.

(I) GeoMx counts for VEGFA and HIF1 α across the progression series.

(J) GSEA biological pathway enrichment analysis using the spatial transcript results in SBT and LGSC-PT in the stromal compartment (Pathway REACTOME, Gene Ontology Biological Processes) on the comparison in (H).

Boxplots show the 25- and 75- percentile and the median value as center line. Whiskers span the 1.5-fold interquartile range, and each data point represents a patient-derived sample. The significance between comparisons was determined using a two-sided Student's *t* test.

Also see Figures S9–S12 and Tables S3 and S4.

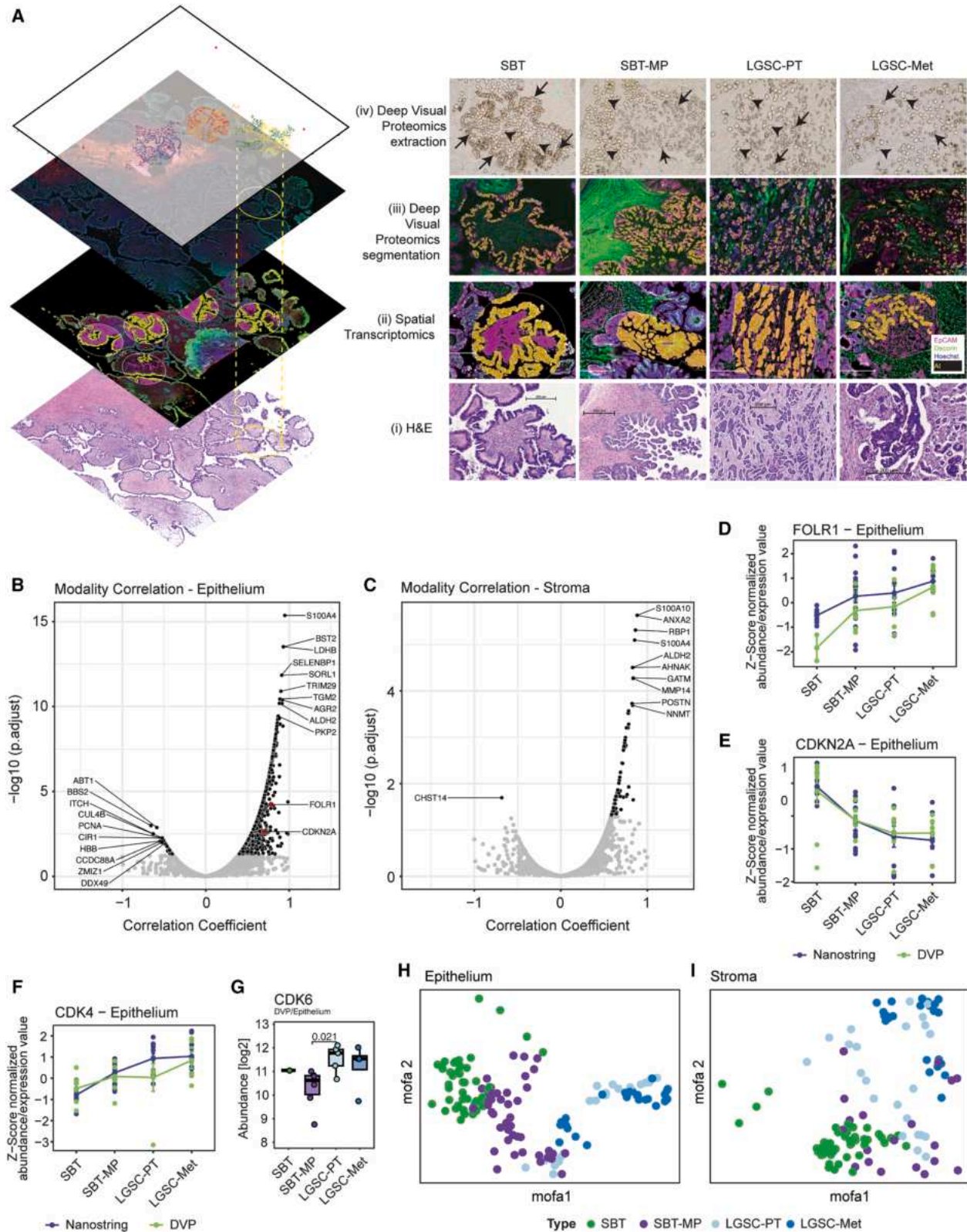


Figure 5. Integration of spatial transcriptomics and proteomics

(A) Multi-layer integration of Deep Visual Proteomics and spatial transcriptomics for the four histologic subtypes. (i) H&E, (ii) spatial transcriptomics regions of interest, (iii) Deep Visual Proteomics including AI-based cell recognition/segmentation, and (iv) brightfield image after DVP laser microdissection.

(legend continued on next page)

(Figure 5) on cancer cell proliferation and invasion. Several FDA-approved inhibitors effectively blocked both proliferation and invasion in LGSC cell lines, including c-MET inhibitors (Savolitinib and Cabozantinib), EGFR inhibitors (Icotinib, Lapatinib, and Erlotinib), CDK inhibitors (Abemaciclib, Milciclib, and Palbociclib), and the MEK inhibitor Trametinib (Figures 7A–7D). The BRAF inhibitor Dabrafenib and the FOLR1-antibody drug conjugate mirvetuximab soravtansine selectively inhibited LGSC cell line proliferation. The selective effect of mirvetuximab soravtansine on cell proliferation but not invasion was consistent with its known mechanism of action targeting tubulin-mediated cell proliferation. The Jun/Fos inhibitor T-5224 reduced VOA6406 proliferation, while the Jak/STAT inhibitor ruxolitinib showed no effect on cancer cell proliferation or invasion (Figures 7A and 7C, S14G, and S14H). In a co-culture experiment with fibroblasts and cancer cells, the MMP2/9 inhibitor, SB3CT, blocked proliferation, while the TGF β R1 inhibitor galunisertib blocked both invasion and proliferation. An α 5 β 1-integrin antibody, IIA1, inhibited invasion in co-culture and when cancer cells were cultured alone (Figures 7B and 7D, S14I, and S14J).

We reasoned that CDK4/6 inhibitors like milciclib, which target dysregulated cell-cycle progression, could synergize with therapy in LGSC directed against FOLR1, which we found prominently expressed in LGSC and its metastasis (Figures 5D, S6B, and S6F). Through *in vivo* passaging of VOA6406 cells in mice we developed a robust murine LGSC model. Administration of mirvetuximab soravtansine and milciclib, as single agents or combined, significantly reduced tumor weight, malignant ascites and the number of metastatic nodules (Figure 7E). Altogether, the pathways identified by combined proteomics and transcriptomics proved therapeutically targetable, demonstrating the translational potential of this multi-omics approach.

DISCUSSION

We performed a detailed analysis of the molecular transition from SBTs through micropapillary SBTs to low-grade serous carcinoma and its corresponding metastasis using cell-type resolved spatial proteomics and transcriptomics. This comprehensive analysis was enabled by the wider availability of spatial transcriptomics and improvements to our recently described DVP technology,^{13,17} including enhanced throughput and refined sample preparation.⁴⁶ This approach identified up to 6,000 proteins in approximately 200 cells across 100 samples.

The tissue-based nature of both DVP and spatial transcriptomics enables the use of serial tissue sections to generate complementary results across two layers of gene expression while maintaining correlation with H&E staining. Our transcriptomics and proteomics analyses captured previously known biological changes in cancer progression. While transcriptomics currently provides greater depth, proteomics offers higher accuracy due to higher resolution between cell types and enables the accurate quantification of protein level changes during progression. Furthermore, proteomics depth and resolution are expected to increase as the technology moves toward single-cell capabilities.⁴⁷

Unlike conventional SBTs, serous borderline tumors with micropapillary features (SBT-MP) frequently affect both ovaries and have a higher risk of recurrence than SBT.⁴⁸ Our proteomic data identified SBT-MP as an intermediate stage between SBT and LGSC, with a proteome that shares features with SBT while exhibiting distinct alterations. Prior studies investigating SBT and LGSC consistently highlighted changes in *RAS* genes, *BRAF*, *ERBB2*, and *NF1*, all regulators of the MAPK pathway, which is altered in more than 50% of all LGSC and borderline tumors.^{23,49} Our results revealed changes in additional targetable components of the MAPK pathways that demonstrated a gradual activation of the entire MAPK network⁵⁰ during tumor transformation. Treatment with FDA-approved *EGFR*, *MEK*, and *BRAF* inhibitors confirmed the functional importance of these pathways in LGSC biology. Our transcriptomics analyses complemented these findings, revealing high expression of *JUNB* and *c-FOS*, family members of the MAPK-regulated transcription factor, *AP-1*. The functional significance of this pathway was demonstrated when treatment with a *c-FOS/AP1* inhibitor blocked proliferation in LGSC cell lines. During metastasis, LGSC tumors developed highly patient-specific proteomic changes, likely driven by the tumor microenvironment of the secondary sites. Nevertheless, specific transcriptional changes in cell dynamics, including the upregulation of the neural axon guidance factor, *SLIT2*, remained consistent across LGSC metastases.

A key strength of this study is the use of epithelial and stromal cells excised from the tumor microenvironment, enabling cell-type-specific resolution. During tumor progression, the stromal compartment undergoes major changes, including the activation of ephrin signaling, which regulates tumor growth through changes in tissue architecture,⁵¹ gluconeogenesis, and angiogenesis driven by *VEGFA* and *HIF1 α* . These findings align with the clinical efficacy of Bevacizumab in LGSC treatment.⁵² We

Immunofluorescence showing malignant epithelial cells (EpCAM, purple) and stroma (decorin, green) in both spatial proteomics and transcriptomics (ii, iii). AI-based recognition in the DVP or Nanostring technology is shown in yellow (tumor compartment) and magenta (stromal compartment in spatial transcriptomics), respectively. Microdissected epithelial cells (black arrows) and stroma (arrowheads) (iv). ROIs of spatial transcriptomics matched to the previously selected regions. The top layer of the visual integration (left panel) shows the laser microdissected cells in different regions for the epithelium (blue/yellow/red) and in the stroma (purple/orange/green) used in DVP. Scale bars: 200 μ m (i); 250 μ m (ii).

(B and C) Correlation of protein and transcript expression comparing spatial proteomics and transcriptomics. Significantly correlated genes are highlighted in black (adj. *p* value \leq 0.05). The top 10 significant correlating and anti-correlating hits are annotated. FOLR1 and CDKN2A are highlighted in red.

(D–F) Z score normalized protein and transcript abundance of FOLR1 (D), CDKN2A (E), and CDK4 (F).

(G) Boxplot (protein abundance) of CDK6.

(H and I) Integration of transcriptomic and proteomic data using the Multi-Omics Factor Analysis (MOFA+) bioinformatic platform, resulting in a distinct separation of cohort groups in cancer epithelium (H) and stroma (I). The MOFA+ platform is a factor analysis that identifies shared or specific patterns (latent factors) supported by feature weight matrices in model training.

Boxplots show the 25- and 75- percentile and the median value as center line. Whiskers span the 1.5-fold interquartile range, and each data point represents a patient-derived sample. The significance between comparisons was determined using a two-sided Student's *t* test.

Also see Figures S13 and Table S3.

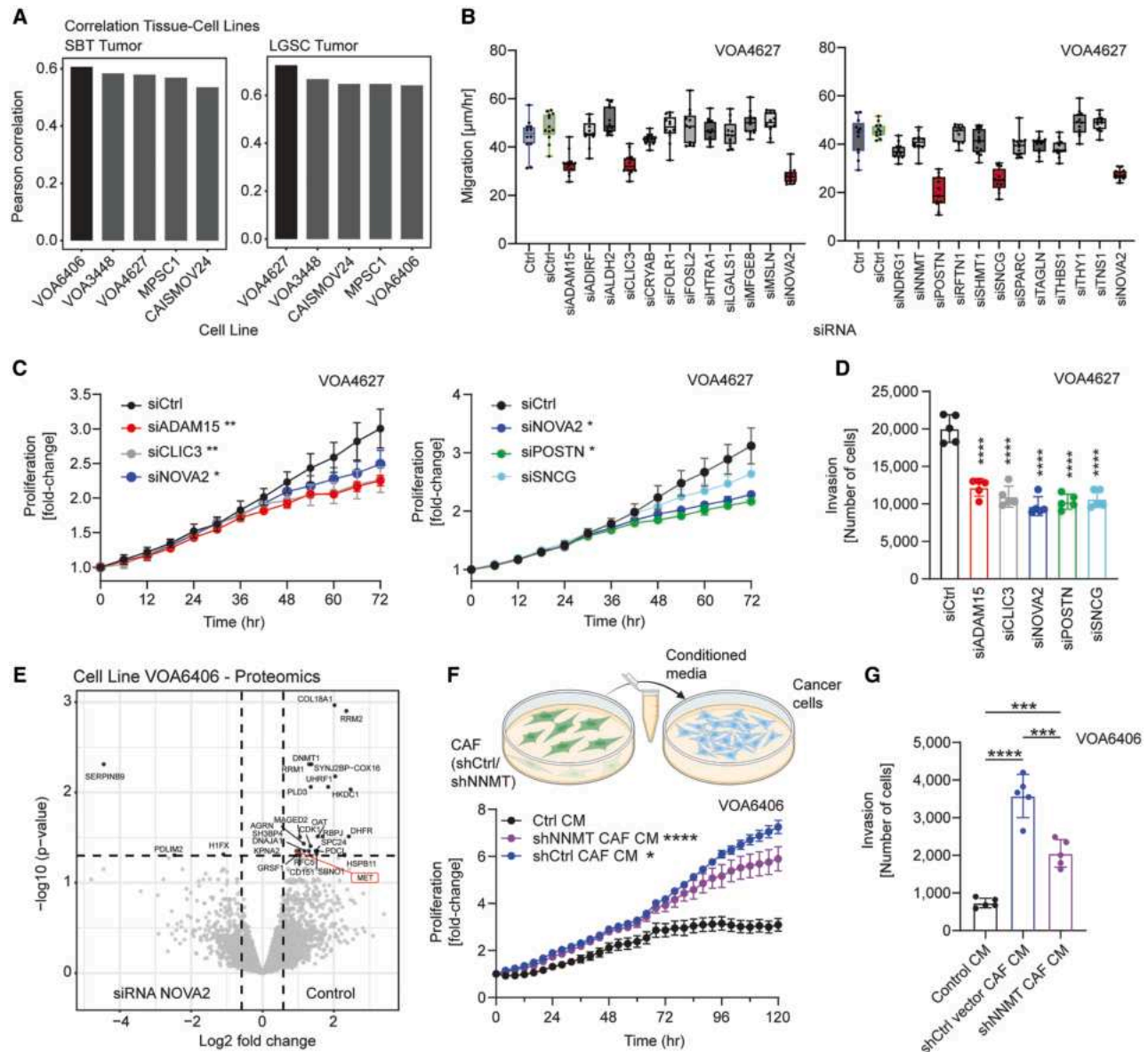


Figure 6. In vitro studies on 'omics'-derived potential drivers in the transitions of SBT to LGSC

(A) LGSC cell lines. Pearson coefficients of the correlation analysis of protein expression (DVP) from SBT (left) and LGSC (right) human epithelial tissue compared to epithelial LGSC cell lines. Cell lines with the highest similarity to human tissue are highlighted in black.

(B) siRNA screening of 23 significantly altered genes using the LGSC cell line VOA4627 measuring cell migration.

(C and D) Validation of the most promising siRNA hits in the LGSC cell line VOA4627 measuring proliferation (C) and invasion (D).

(E) MS-based proteomics. Differential expression between the siRNA NOVA2 knock-down versus control in the VOA6406 cell lines. A fold change cutoff of 1.5 and a q-value cutoff of 0.05 are indicated by vertical and horizontal lines, respectively. Proteins matching the significance for differential regulation criteria are highlighted in black. The correlation of c-MET proteome abundance with NOVA2 expression is red.

(F and G) Inhibition of NNMT in cancer-associated fibroblasts (CAFs) reduces epithelial cell proliferation and invasion. VOA6406 LGSC epithelial cells were treated with either conditioned media from immortalized human CAFs where NNMT knock-down was accomplished using shRNA (shNNMT CAF CM), shRNA control transfected CAF condition media (shCtrl CAF CM), or control media (Ctrl M). A proliferation (F) and invasion (G) assay show a negative impact on cell proliferation and invasion without NNMT.

Boxplots show the 25- to 75-percentile and the median value as center line. Whiskers span the 1.5-fold interquartile range, and each data point represents a replicate of the growth of the respective cell line. All growth curves and bar graphs show mean \pm SEM. The data presented in (C, D, and F) was repeated in three independent experiments. Significance levels were determined by one-way ANOVA analysis. *p*-value: * <0.05, ** <0.01, *** <0.001, **** <0.0001.

Also see [Figures S14](#) and [Table S3](#).

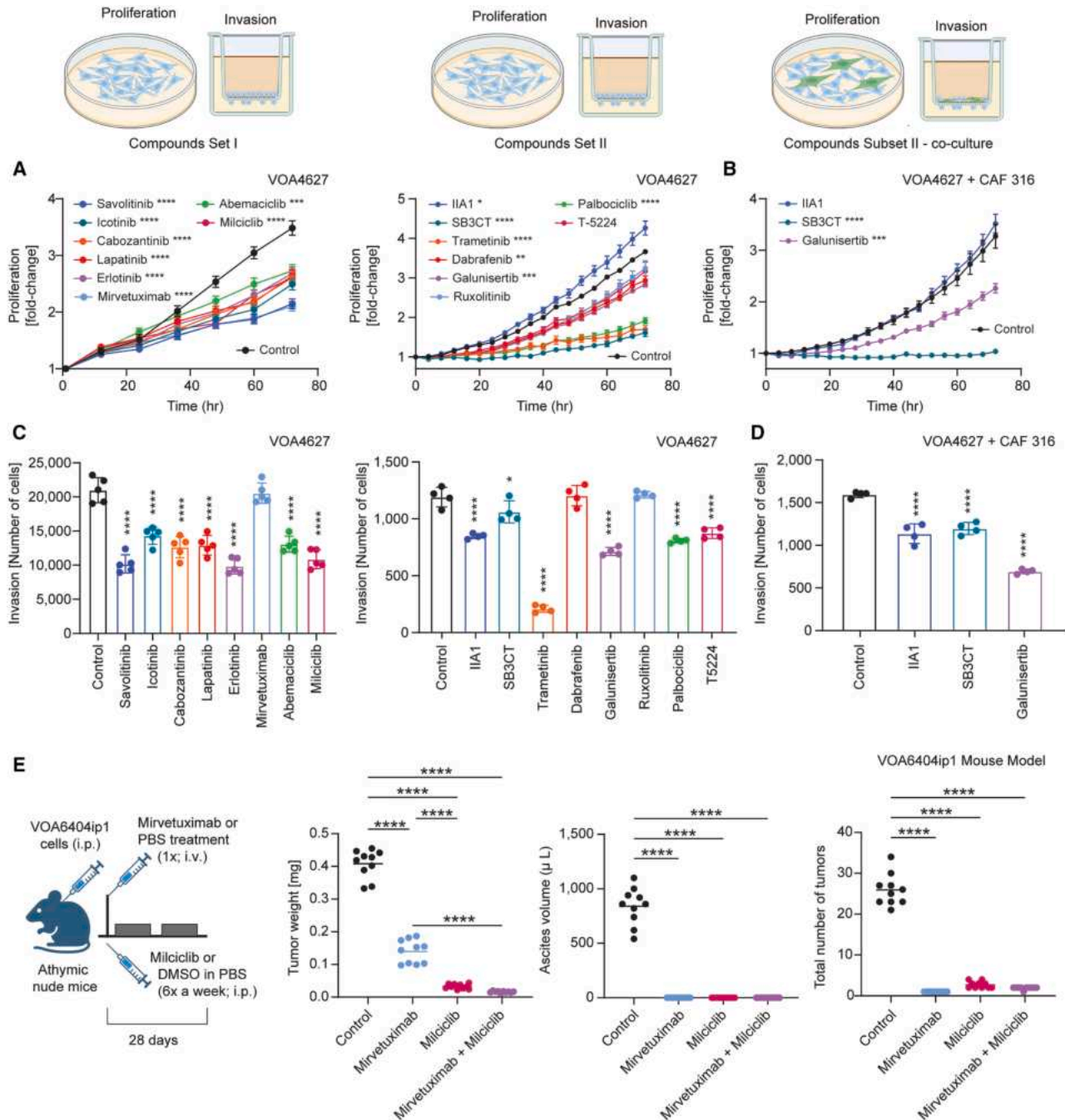


Figure 7. Evaluation of new therapeutic strategies in low-grade serous ovarian cancer

(A–D) *In vitro* evaluation of either FDA-approved or clinical-stage compounds in VOA4627 cells. Cell proliferation (A) and invasion (C) are shown for compound treatment of epithelial cancer cells alone as well as co-cultures with immortalized primary human ovarian CAFs for ECM-associated inhibitors (B and D).

(E) *In vivo* evaluation of the CDK inhibitor miliciclib and the FOLR1-targeting mirvetuximab soravtansine alone or in combination treatment. Nude mice were injected with VOA6404ip1 cells intraperitoneal (i.p.) on day 1. Treatment was initiated on day 14 with a one-time intravenous treatment of mirvetuximab soravtansine or PBS control, followed by i.p. treatment of miliciclib or DMSO control on days 15–20 and 22–27. Tumor weight (left), ascites volume (middle), and total number of tumors (right) were recorded. Each point in the graph corresponds to one mouse. Line, mean.

All growth curves and bar graphs show mean \pm SEM. The data presented in a–d was repeated in 3 independent experiments. Significance levels were determined by one-way ANOVA analysis. *p*-value: ** <0.01, *** <0.001, **** <0.0001.

Also see [Figures S14](#) and [Table S3](#).

found closer interactions between epithelial tumor and stromal cells in LGSC than in SBT. Increased levels of cell adhesion proteins, including $\alpha 5$ -integrin and $\beta 1$ -integrin receptors and their ligand fibronectin (*FN1*), help stabilize epithelial tumor cells in the extracellular matrix of LGSC following dissociation from SBT epithelial cell clusters.⁵³ Additionally, tumor cell dissociation and invasion through the ECM are likely facilitated by the increased release of metalloproteinases, which are established modulators of the tumor environment.⁵⁴ *In vitro* co-culture experiments demonstrated that *MMP2/9* inhibition directly decreased cell proliferation, while $\alpha 5\beta 1$ -integrin blockage inhibits cell invasion. The most prominent single protein and transcript change in the stroma during tumor progression was the abundance of the methyltransferase, *NNMT*, which reprograms normal fibroblasts into CAFs by affecting methylation.³⁷ *NNMT* knockdown in primary human fibroblasts blocked both invasion and proliferation of epithelial tumor cells, suggesting that stromal-directed treatment approaches could be of therapeutic value.

To integrate spatial proteomics and transcriptomics, we employed the recent statistical framework MOFA+, a scalable platform for state-of-the-art analysis of complex multi-omics data.⁴³ We used an integrated panel of the most significantly changed proteins/transcripts and complementary literature-validated targets from our data to guide the downstream functional experiments investigating the molecular drivers of invasive ovarian cancer progression. Through these post-hoc validation and functional studies, we identified five previously unknown molecular players in LGSC: *CLIC3*, *POSTN*, *ADAM15*, *SNCG*, and *NOVA2*. Among those, a knock-down of the typically stromal proteins *POSTN* and *ADAM15* altered the tumor cell invasiveness, suggesting a dual role for these proteins in the stromal and epithelial compartments. The brain-specific splicing regulator, *NOVA2*, showed high expression in the proteome of LGSC and its corresponding metastasis but was completely absent in SBT and SBT-MP. Proteomic analysis following knock-down of *NOVA-2* identified c-Met as one of the most altered proteins.⁵⁵ Subsequent inhibition of c-Met with several FDA-approved inhibitors produced a strong reduction in cell migration and invasion, revealing another potential therapeutic strategy. Additionally, *NOVA2* regulates fibronectin (*FN1*) splicing, which embeds tumor cells in the stromal environment.⁵⁶ *NOVA2* was detected at the protein level but not in the transcriptome, underscoring the importance of complementary omics approaches. The discovery of *NOVA2* alongside other neuronal proteins and transcripts, such as *SNCG* and the neural axon guidance factor *SLIT2*, suggests a correlation between neuronal (dynamic) processes in LGSC and invasion into the microenvironment.

Our integrated omics analysis revealed upregulation of CDK signaling, including *CDK4/6*, along with high expression levels of *FOLR1*. Using a new mouse model that recapitulates the biology of LGSC, we found that an antibody-drug conjugate approved for advanced HGSC treatment, mirvetuximab soravtansine, and the CDK4/6 inhibitor, milciclib, each significantly reduced tumor growth and expansion and showed additive effects when combined.^{57,58} While mirvetuximab soravtansine and milciclib are both FDA-approved and in clinical trials for several cancer indications, they have not yet been used in low-grade serous cancer (LGSC). Our data strongly supports the clinical development of both compounds in advanced LGSC.

This work presents the first multi-omic spatial atlas of low-grade serous ovarian cancer progression. It molecularly characterizes a previously hypothetical transition pathway, reveals numerous functionally important proteins and pathways, and identifies novel treatment targets. Our comprehensive characterization of the molecular landscape of SBTs and LGSC through two omics approaches and genomic analysis not only provides an in-depth resource for further disease analyses but also presents findings with translational relevance. Furthermore, the methodological approach developed for studying LGSC offers a blueprint for investigating other cancers or diseases where the multi-modal, cellular, and spatially resolved analysis of benign to malignant transitions would prove beneficial.

Limitations of the study

Genomic sequencing data on each patient of this study adds an additional layer of omics information. Every patient had a different mutational pattern, which contributed to the heterogeneity of the cohort. While using individual matching data allows the direct correlation of genetic alterations and transcript/protein expression, the heterogeneous genetic profile of different patients and disease stages affected the overall data integration. Despite patient heterogeneity, the results show significant changes in transcriptomic and proteomic patterns that enable novel insights into LGSC biology which may inform future clinical trial concepts. Larger patient cohorts may allow the identification of transcriptomic/proteomic alterations for each genetic subgroup in SBT and LGSC (e.g., high versus low MAPK tumor expression).

RESOURCE AVAILABILITY

Lead contact

Requests for further information and resources should be directed to and will be fulfilled by the lead contact, Ernst Lengyel (elengyel@uchicago.edu).

Materials availability

This study did not generate new unique reagents.

Data and code availability

Pseudonymized MS-based proteomics data of this study have been deposited to the ProteomeXchange Consortium via the PRIDE⁵⁹ partner repository (PRIDE: PXD046354). Pseudonymized GeoMx spatial transcriptomics files have been submitted to the GEO archive (GEO accession GSE289044). These data will be publicly available upon the publication of this work.

ACKNOWLEDGMENTS

We want to thank Dr. Annette Feuchtinger and her team from the Core Facility Pathology & Tissue Analytics at the Helmholtz Center, Munich, Germany, for their support during image data acquisition; Dirk Wischniewski (MPI Munich), Destiny Brown (U of C) and Paul Miller (U of C) for technical support; members of the Department of Proteomics and Signal Transduction at the Max Planck of Biochemistry in Munich, Germany; the members of the Ovarian Cancer Research Laboratory at The University of Chicago, USA, as well as members from the Center for Protein Research at Copenhagen University, Denmark, for fruitful discussions.

We thank Pieter Farber, Ph.D., from the U of C Genomics facility for help with the spatial transcriptomics; Jeremy Segal, Ph.D., and Melissa Tjota with the genomic analysis of our patient cohort. We also thank Dr. Mark Carey (The University of British Columbia, Division of Gynecologic Oncology, USA), Dr. Ie-Ming Shih (The Johns Hopkins Hospital, Department of Pathology, USA), and Dr. Fernando Guimarães (University of Campinas, Experimental Pathology Laboratory, Brazil) for low-grade cancer cell lines. We thank Robert

Darnell and Erin Conlon for sharing their ideas and expertise on neuro-oncology. We thank Qiaoshan Lin (U of C, Center for Research Informatics) for her support with data management. We thank Gail Isenberg (U of C, OB/GYN department) for editing the manuscript.

This research has been supported by generous philanthropic gifts from Linda Usher and her family (SD Yamada), Bears Care – the charitable beneficiary of the Chicago Bears Football Club (H. Kenny and E. Lengyel), the Janet Burros Memorial Foundation (E. Lengyel), and an NIH/NCI R35 grant (CA264619, E Lengyel). The Cellular Screening Center and Human Tissue Resource Center Cores at the University of Chicago are funded by the Cancer Center Support Grant (P30CA014599). Furthermore, this study was supported by the Max Planck Society for Advancement of Science (M. Mann). L. Schweizer acknowledges funding from the German Federal Ministry of Education and Research under the funding code 16LW0243K. L. Schweizer and M. Thielert were supported by the International Max Planck Research School for Life Sciences – IMPRS-LS. F.A. Rosenberger is an EMBO postdoctoral fellow (ALTF 399-2021), and T.M. Nordmann is supported by a Swiss National Science Foundation (SNSF) Early Postdoc Mobility (P2ZHP3-199648) and Postdoc Mobility Fellowship (P500PM_210917). M. Thielert was supported by the European Union's Horizon 2020 research and innovation program under grant agreement No. 874839 (ISLET). S. Richter is supported by the Helmholtz Association under the joint research school "Munich School for Data Science" –MUDS.

AUTHOR CONTRIBUTIONS

The study was conceived by E.L. and M.M. Deep Visual Proteomics (DVP) application, data acquisition and interpretation were performed by L.S., R. K., and A. Metousis with the support of M.T., T.M.N., F.A.R., and E.R. Spatial transcriptomics data were acquired by R.K., L.S., and A.J.B. Omics data were statistically evaluated and interpreted by L.S., M.S., and J.B.M.-R. Advanced data integration and deconvolution were performed by Y.L. and L.D. as well as S.R. under supervision of F.J.T. The patient cohort was identified by E.L., R.M., S.D.Y., K.C.K., R.K., A.J.B. and R.R.L. Pathological expertise was provided by R.M., R.R.L., and A.J.B. Functional experiments were designed by A.S., H.A. K., L.S., J.H., and E.L., and performed by L.K., H.A.K., A.S., S.R., and J.H. Mice experiments were performed by H.A.K.; A.J.B. completed all immunohistochemistry stainings. L.S. prepared all the figures. L.S. and E.L. wrote the paper. H.A.K., A. Mund, J.H., and M.M. edited the manuscript. All authors reviewed, provided feedback, and approved the final resubmitted version.

The presented work was part of the Ph.D. thesis of L.S.

DECLARATION OF INTERESTS

E.L. receives research funding to study the biology of ovarian cancer from AbbVie through the University of Chicago, which is unrelated to this work. L. S. is a current employee of OmicVision Biosciences ApS; M.S. and A. Mund are co-founders and shareholders of OmicVision Biosciences ApS. F.J.T. consults for Immunai Inc., Singularity Bio B.V., CytoReason Ltd, Cellarity, and has ownership interest in Dermagnostix GmbH and Cellarity. M.M. is an indirect investor in Evosep and OmicVision Biosciences ApS. The other authors declare no potential conflicts of interest in the context of this manuscript.

STAR★METHODS

Detailed methods are provided in the online version of this paper and include the following:

- **KEY RESOURCES TABLE**
- **EXPERIMENTAL MODEL AND STUDY PARTICIPANT DETAILS**
 - Patient cohort, ethics and inclusion statement
 - Mouse models
 - Cell lines
- **METHOD DETAILS**
 - Deep Visual Proteomics
 - Bulk proteomics of cell lines
 - GeoMx spatial transcriptomics
 - Advanced data integration
 - Antibody-based validation staining

- siRNA transfection
- Inhibitor testing
- Quantitative PCR with reverse transcription
- Genomic sequencing
- Functional assays

● QUANTIFICATION AND STATISTICAL ANALYSIS

SUPPLEMENTAL INFORMATION

Supplemental information can be found online at <https://doi.org/10.1016/j.ccell.2025.06.004>.

Received: July 1, 2024

Revised: February 28, 2025

Accepted: June 3, 2025

REFERENCES

1. Slomovitz, B., Gourley, C., Carey, M.S., Malpica, A., Shih, I.M., Huntsman, D., Fader, A.N., Grisham, R.N., Schlumbrecht, M., Sun, C.C., et al. (2020). Low-grade serous ovarian cancer: State of the science. *Gynecol. Oncol.* *156*, 715–725. <https://doi.org/10.1016/j.ygyno.2019.12.033>.
2. Kelliher, L., Yoeli-Bik, R., Schweizer, L., and Lengyel, E. (2024). Molecular changes driving low-grade serous ovarian cancer and implications for treatment. *Int. J. Gynecol. Cancer* *34*, 1630–1638. <https://doi.org/10.1136/ijgc-2024-005305>.
3. Gershenson, D.M., Sun, C.C., Bodurka, D., Coleman, R.L., Lu, K.H., Sood, A.K., Deavers, M., Malpica, A.L., and Kavanagh, J.J. (2009). Recurrent low-grade serous ovarian carcinoma is relatively chemoresistant. *Gynecol. Oncol.* *114*, 48–52. <https://doi.org/10.1016/j.ygyno.2009.03.001>.
4. Kurnit, K.C., Fleming, G.F., and Lengyel, E. (2021). Updates and New Options in Advanced Epithelial Ovarian Cancer Treatment. *Obstet. Gynecol.* *137*, 108–121. <https://doi.org/10.1097/AOG.0000000000004173>.
5. Singer, G., Stöhr, R., Cope, L., Dehari, R., Hartmann, A., Cao, D.F., Wang, T.L., Kurman, R.J., and Shih, I.M. (2005). Patterns of p53 mutations separate ovarian serous borderline tumors and low- and high-grade carcinomas and provide support for a new model of ovarian carcinogenesis: A mutational analysis with immunohistochemical correlation. *Am. J. Surg. Pathol.* *29*, 218–224.
6. Tang, M., O'Connell, R.L., Amant, F., Beale, P., McNally, O., Sjoquist, K. M., Grant, P., Davis, A., Sykes, P., Mileskin, L., et al. (2019). PARAGON: A Phase II study of anastrozole in patients with estrogen receptor-positive recurrent/metastatic low-grade ovarian cancers and serous borderline ovarian tumors. *Gynecol. Oncol.* *154*, 531–538. <https://doi.org/10.1016/j.ygyno.2019.06.011>.
7. Ho, C.L., Kurman, R.J., Dehari, R., Wang, T.L., and Shih, I.M. (2004). Mutations of BRAF and KRAS precede the development of ovarian serous borderline tumors. *Cancer Res.* *64*, 6915–6918. <https://doi.org/10.1158/0008-5472.CAN-04-2067>.
8. Anglesio, M.S., Arnold, J.M., George, J., Tinker, A.V., Tothill, R., Waddell, N., Simms, L., Locandro, B., Fereday, S., Traficante, N., et al. (2008). Mutation of ERBB2 provides a novel alternative mechanism for the ubiquitous activation of RAS-MAPK in ovarian serous low malignant potential tumors. *Mol. Cancer Res.* *6*, 1678–1690. <https://doi.org/10.1158/1541-7786.MCR-08-0193>.
9. Manning-Geist, B., Gordhandas, S., Liu, Y.L., Zhou, Q., Iasonos, A., Da Cruz Paula, A., Mandelker, D., Long Roche, K., Zivanovic, O., Maio, A., et al. (2022). MAPK Pathway Genetic Alterations Are Associated with Prolonged Overall Survival in Low-Grade Serous Ovarian Carcinoma. *Clin. Cancer Res.* *28*, 4456–4465. <https://doi.org/10.1158/1078-0432.CCR-21-4183>.
10. Silva, E.G., Lawson, B.C., Ramalingam, P., Liu, J., Shehabeldin, A., Marques-Piubelli, M.L., and Malpica, A. (2022). Precursors in the ovarian stroma: another pathway to explain the origin of ovarian serous neoplasms. *Hum. Pathol.* *127*, 136–145. <https://doi.org/10.1016/j.humpath.2022.04.008>.

11. Vang, R., Hannibal, C.G., Junge, J., Frederiksen, K., Kjaer, S.K., and Kurman, R.J. (2017). Long-term Behavior of Serous Borderline Tumors Subdivided Into Atypical Proliferative Tumors and Noninvasive Low-grade Carcinomas: A Population-based Clinicopathologic Study of 942 Cases. *Am. J. Surg. Pathol.* *41*, 725–737. <https://doi.org/10.1097/PAS.0000000000000824>.
12. Lengyel, E. (2010). Ovarian cancer development and metastasis. *Am. J. Pathol.* *177*, 1053–1064. <https://doi.org/10.2353/ajpath.2010.100105>.
13. Mund, A., Coscia, F., Kriston, A., Hollandi, R., Kovács, F., Brunner, A.D., Migh, E., Schweizer, L., Santos, A., Bzorek, M., et al. (2022). Deep Visual Proteomics defines single-cell identity and heterogeneity. *Nat. Biotechnol.* *40*, 1231–1240. <https://doi.org/10.1038/s41587-022-01302-5>.
14. Shih, I.M., Wang, Y., and Wang, T.L. (2021). The Origin of Ovarian Cancer Species and Precancerous Landscape. *Am. J. Pathol.* *191*, 26–39. <https://doi.org/10.1016/j.ajpath.2020.09.006>.
15. Hollandi, R., Szkalitsy, A., Toth, T., Tasnadi, E., Molnar, C., Mathe, B., Grexa, I., Molnar, J., Balind, A., Gorbe, M., et al. (2020). nucleAlzer: A Parameter-free Deep Learning Framework for Nucleus Segmentation Using Image Style Transfer. *Cell Syst.* *10*, 453–458.e6. <https://doi.org/10.1016/j.cels.2020.04.003>.
16. Makhmut, A., Qin, D., Fritzsche, S., Nimo, J., König, J., and Coscia, F. (2023). A framework for ultra-low-input spatial tissue proteomics. *Cell Syst.* *14*, 1002–1014.e5. <https://doi.org/10.1016/j.cels.2023.10.003>.
17. Nordmann, T.M., Anderton, H., Hasegawa, A., Schweizer, L., Zhang, P., Stadler, P.C., Sinha, A., Metousis, A., Rosenberger, F.A., Zwiebel, M., et al. (2024). Spatial proteomics identifies JAKi as treatment for a lethal skin disease. *Nature* *635*, 1001–1009. <https://doi.org/10.1038/s41586-024-08061-0>.
18. Scott, B.J., Qutob, S., Liu, Q.Y., and Ng, C.E. (2009). APM2 is a novel mediator of cisplatin resistance in a variety of cancer cell types regardless of p53 or MMR status. *Int. J. Cancer* *125*, 1193–1204. <https://doi.org/10.1002/ijc.24465>.
19. Hunter, S.M., Anglesio, M.S., Ryland, G.L., Sharma, R., Chiew, Y.E., Rowley, S.M., Doyle, M.A., Li, J., Gilks, C.B., Moss, P., et al. (2015). Molecular profiling of low grade serous ovarian tumours identifies novel candidate driver genes. *Oncotarget* *6*, 37663–37677. <https://doi.org/10.18632/oncotarget.5438>.
20. Wang, Y., Dan, L., Li, Q., Li, L., Zhong, L., Shao, B., Yu, F., He, S., Tian, S., He, J., et al. (2019). ZMYND10, an epigenetically regulated tumor suppressor, exerts tumor-suppressive functions via miR145-5p/NEDD9 axis in breast cancer. *Clin. Epigenetics* *11*, 184. <https://doi.org/10.1186/s13148-019-0785-z>.
21. Yi, M., Yang, J., Li, W., Li, X., Xiong, W., McCarthy, J.B., Li, G., and Xiang, B. (2017). The NOR1/OSCP1 proteins in cancer: from epigenetic silencing to functional characterization of a novel tumor suppressor. *J. Cancer* *8*, 626–635. <https://doi.org/10.7150/jca.17579>.
22. King, E.R., Tung, C.S., Tsang, Y.T.M., Zu, Z., Lok, G.T.M., Deavers, M.T., Malpica, A., Wolf, J.K., Lu, K.H., Birrer, M.J., et al. (2011). The anterior gradient homolog 3 (AGR3) gene is associated with differentiation and survival in ovarian cancer. *Am. J. Surg. Pathol.* *35*, 904–912. <https://doi.org/10.1097/PAS.0b013e318212ae22>.
23. Gershenson, D.M., Sun, C.C., Westin, S.N., Eyada, M., Cobb, L.P., Nathan, L.C., Sood, A.K., Malpica, A., Hillman, R.T., and Wong, K.K. (2022). The genomic landscape of low-grade serous ovarian/peritoneal carcinoma and its impact on clinical outcomes. *Gynecol. Oncol.* *165*, 560–567. <https://doi.org/10.1016/j.ygyno.2021.11.019>.
24. Xu, M., Zhou, H., Zhang, C., He, J., Wei, H., Zhou, M., Lu, Y., Sun, Y., Ding, J.W., Zeng, J., et al. (2016). ADAM17 promotes epithelial-mesenchymal transition via TGF-beta/Smad pathway in gastric carcinoma cells. *Int. J. Oncol.* *49*, 2520–2528. <https://doi.org/10.3892/ijo.2016.3744>.
25. Moreau, J.M., Velegraki, M., Bolyard, C., Rosenblum, M.D., and Li, Z. (2022). Transforming growth factor-beta1 in regulatory T cell biology. *Sci. Immunol.* *7*, eabi4613. <https://doi.org/10.1126/sciimmunol.abi4613>.
26. Llaurado Fernandez, M., Dawson, A., Kim, H., Lam, N., Russell, H., Bruce, M., Bittner, M., Hoenisch, J., Scott, S.A., Talhouk, A., et al. (2020). Hormone receptor expression and outcomes in low-grade serous ovarian carcinoma. *Gynecol. Oncol.* *157*, 12–20. <https://doi.org/10.1016/j.ygyno.2019.11.029>.
27. Saito, Y., Yuan, Y., Zucker-Scharff, I., Fak, J.J., Jereb, S., Tajima, Y., Licatalosi, D.D., and Darnell, R.B. (2019). Differential NOVA2-Mediated Splicing in Excitatory and Inhibitory Neurons Regulates Cortical Development and Cerebellar Function. *Neuron* *101*, 707–720.e5. <https://doi.org/10.1016/j.neuron.2018.12.019>.
28. Kimura, I., Konishi, M., Miyake, A., Fujimoto, M., and Itoh, N. (2006). Neudesin, a secreted factor, promotes neural cell proliferation and neuronal differentiation in mouse neural precursor cells. *J. Neurosci. Res.* *83*, 1415–1424. <https://doi.org/10.1002/jnr.20849>.
29. Zou, H., Wen, C., Peng, Z., Shao, Y.Y., Hu, L., Li, S., Li, C., and Zhou, H.H. (2018). P4HB and PDIA3 are associated with tumor progression and therapeutic outcome of diffuse gliomas. *Oncol. Rep.* *39*, 501–510. <https://doi.org/10.3892/or.2017.6134>.
30. Turei, D., Korcsmaros, T., and Saez-Rodriguez, J. (2016). OmniPath: guidelines and gateway for literature-curated signaling pathway resources. *Nat. Methods* *13*, 966–967. <https://doi.org/10.1038/nmeth.4077>.
31. Noye, T.M., Lokman, N.A., Oehler, M.K., and Ricciardelli, C. (2018). S100A10 and Cancer Hallmarks: Structure, Functions, and its Emerging Role in Ovarian Cancer. *Int. J. Mol. Sci.* *19*, 4122. <https://doi.org/10.3390/ijms19124122>.
32. Truebestein, L., Elsner, D.J., Fuchs, E., and Leonard, T.A. (2015). A molecular ruler regulates cytoskeletal remodelling by the Rho kinases. *Nat. Commun.* *6*, 10029. <https://doi.org/10.1038/ncomms10029>.
33. Su, G., Blaine, S.A., Qiao, D., and Friedl, A. (2008). Membrane type 1 matrix metalloproteinase-mediated stromal syndecan-1 shedding stimulates breast carcinoma cell proliferation. *Cancer Res.* *68*, 9558–9565. <https://doi.org/10.1158/0008-5472.CAN-08-1645>.
34. Kenny, H.A., Kaur, S., Coussens, L.M., and Lengyel, E. (2008). The initial steps of ovarian cancer cell metastasis are mediated by MMP-2 cleavage of vitronectin and fibronectin. *J. Clin. Investig.* *118*, 1367–1379. <https://doi.org/10.1172/JCI33775>.
35. Nyalali, A.M.K., Leonard, A.U., Xu, Y., Li, H., Zhou, J., Zhang, X., Rugambwa, T.K., Shi, X., and Li, F. (2023). CD147: an integral and potential molecule to abrogate hallmarks of cancer. *Front. Oncol.* *13*, 1238051. <https://doi.org/10.3389/fonc.2023.1238051>.
36. Wang, Z., and Dong, C. (2019). Glucocorticoidogenesis in Cancer: Function and Regulation of PEPCCK, FBPase, and G6Pase. *Trends Cancer* *5*, 30–45. <https://doi.org/10.1016/j.trecan.2018.11.003>.
37. Eckert, M.A., Coscia, F., Chryplewicz, A., Chang, J.W., Hernandez, K.M., Pan, S., Tienda, S.M., Nahotko, D.A., Li, G., Blaženović, I., et al. (2019). Proteomics reveals NNMT as a master metabolic regulator of cancer-associated fibroblasts. *Nature* *569*, 723–728. <https://doi.org/10.1038/s41586-019-1173-8>.
38. White, N.M.A., Mathews, M., Yousef, G.M., Prizada, A., Popadiuk, C., and Doré, J.J.E. (2009). KLK6 and KLK13 predict tumor recurrence in epithelial ovarian carcinoma. *Br. J. Cancer* *101*, 1107–1113. <https://doi.org/10.1038/sj.bjc.6605280>.
39. Hendrickson, P.G., Doráis, J.A., Grow, E.J., Whiddon, J.L., Lim, J.W., Wike, C.L., Weaver, B.D., Pflueger, C., Emery, B.R., Wilcox, A.L., et al. (2017). Conserved roles of mouse DUX and human DUX4 in activating cleavage-stage genes and MERVL/HERVL retrotransposons. *Nat. Genet.* *49*, 925–934. <https://doi.org/10.1038/ng.3844>.
40. Javellana, M., Eckert, M.A., Heide, J., Zawieracz, K., Weigert, M., Ashley, S., Stock, E., Chapel, D., Huang, L., Yamada, S.D., et al. (2022). Neoadjuvant Chemotherapy Induces Genomic and Transcriptomic Changes in Ovarian Cancer. *Cancer Res.* *82*, 169–176. <https://doi.org/10.1158/0008-5472.CAN-21-1467>.
41. de Visser, K.E., and Joyce, J.A. (2023). The evolving tumor microenvironment: From cancer initiation to metastatic outgrowth. *Cancer Cell* *41*, 374–403. <https://doi.org/10.1016/j.ccell.2023.02.016>.

42. Matulonis, U.A., Lorusso, D., Oaknin, A., Pignata, S., Dean, A., Denys, H., Colombo, N., Van Gorp, T., Konner, J.A., Marin, M.R., et al. (2023). Efficacy and Safety of Mirvetuximab Soravtansine in Patients With Platinum-Resistant Ovarian Cancer With High Folate Receptor Alpha Expression: Results From the SORAYA Study. *J. Clin. Oncol.* *41*, 2436–2445. <https://doi.org/10.1200/JCO.22.01900>.
43. Argelaguet, R., Arnol, D., Bredikhin, D., Deloro, Y., Velten, B., Marioni, J.C., and Stegle, O. (2020). MOFA+: a statistical framework for comprehensive integration of multi-modal single-cell data. *Genome Biol.* *20200511*.
44. Newman, A.M., Steen, C.B., Liu, C.L., Gentles, A.J., Chaudhuri, A.A., Scherer, F., Khodadoust, M.S., Esfahani, M.S., Luca, B.A., Steiner, D., et al. (2019). Determining cell type abundance and expression from bulk tissues with digital cytometry. *Nat. Biotechnol.* *37*, 773–782. <https://doi.org/10.1038/s41587-019-0114-2>.
45. Lengyel, E., Li, Y., Weigert, M., Zhu, L., Eckart, H., Javellana, M., Ackroyd, S., Xiao, J., Olalekan, S., Glass, D., et al. (2022). A molecular atlas of the human postmenopausal fallopian tube and ovary from single-cell RNA and ATAC sequencing. *Cell Rep.* *41*, 111838. <https://doi.org/10.1016/j.celrep.2022.111838>.
46. Nordmann, T.M., Schweizer, L., Metousis, A., Thielert, M., Rodriguez, E., Rahbek-Gjerdum, L.M., Stadler, P.C., Bzorek, M., Mund, A., Rosenberger, F.A., and Mann, M. (2023). A standardized and reproducible workflow for membrane glass slides in routine histology and spatial proteomics. *Mol. Cell. Proteomics* *22*, 100643. <https://doi.org/10.1016/j.mcpro.2023.100643>.
47. Rosenberger, F.A., Thielert, M., Strauss, M.T., Schweizer, L., Ammar, C., Madler, S.C., Metousis, A., Skowronek, P., Wahle, M., Madden, K., et al. (2023). Spatial single-cell mass spectrometry defines zonation of the hepatocyte proteome. *Nat. Methods* *20*, 1530–1536. <https://doi.org/10.1038/s41592-023-02007-6>.
48. Longacre, T.A., McKenney, J.K., Tazelaar, H.D., Kempson, R.L., and Hendrickson, M.R. (2005). Ovarian serous tumors of low malignant potential (borderline tumors): outcome-based study of 276 patients with long-term (> or =5-year) follow-up. *Am. J. Surg. Pathol.* *29*, 707–723. <https://doi.org/10.1097/01.pas.0000164030.82810.db>.
49. Etemadmoghadam, D., Azar, W.J., Lei, Y., Moujaber, T., Garsed, D.W., Kennedy, C.J., Fereday, S., Mitchell, C., Chiew, Y.E., Hendley, J., et al. (2017). EIF1AX and NRAS Mutations Co-occur and Cooperate in Low-Grade Serous Ovarian Carcinomas. *Cancer Res.* *77*, 4268–4278. <https://doi.org/10.1158/0008-5472.CAN-16-2224>.
50. Dhillon, A.S., Hagan, S., Rath, O., and Kolch, W. (2007). MAP kinase signalling pathways in cancer. *Oncogene* *26*, 3279–3290. <https://doi.org/10.1038/sj.onc.1210421>.
51. Pasquale, E.B. (2024). Eph receptors and ephrins in cancer progression. *Nat. Rev. Cancer* *24*, 5–27. <https://doi.org/10.1038/s41568-023-00634-x>.
52. Musacchio, L., Turinetti, M., Arenare, L., Bartoletti, M., Califano, D., Tuninetti, V., Marchetti, C., Cormio, G., Loizzi, V., Pisano, C., et al. (2023). Effect of bevacizumab in advanced low grade serous ovarian cancer: Data from the MITO 22 trial. *Gynecol. Oncol.* *172*, 72–77. <https://doi.org/10.1016/j.ygyno.2023.03.011>.
53. Miroshnikova, Y.A., Rozenberg, G.I., Cassereau, L., Pickup, M., Mouw, J. K., Ou, G., Templeman, K.L., Hannachi, E.I., Gooch, K.J., Sarang-Sieminski, A.L., et al. (2017). alpha5beta1-Integrin promotes tension-dependent mammary epithelial cell invasion by engaging the fibronectin synergy site. *Mol. Biol. Cell* *28*, 2958–2977. <https://doi.org/10.1091/mbc.E17-02-0126>.
54. Kessenbrock, K., Plaks, V., and Werb, Z. (2010). Matrix metalloproteinases: regulators of the tumor microenvironment. *Cell* *141*, 52–67. <https://doi.org/10.1016/j.cell.2010.03.015>.
55. Sawada, K., Radjabi, A.R., Shinomiya, N., Kistner, E., Kenny, H., Becker, A.R., Turkyilmaz, M.A., Salgia, R., Yamada, S.D., Vande Woude, G.F., et al. (2007). c-Met overexpression is a prognostic factor in ovarian cancer and an effective target for inhibition of peritoneal dissemination and invasion. *Cancer Res.* *67*, 1670–1679. <https://doi.org/10.1158/0008-5472.CAN-06-1147>.
56. Kenny, H.A., Chiang, C.Y., White, E.A., Schryver, E.M., Habis, M., Romero, I.L., Ladanyi, A., Penicka, C.V., George, J., Matlin, K., et al. (2014). Mesothelial cells promote early ovarian cancer metastasis through fibronectin secretion. *J. Clin. Investig.* *124*, 4614–4628. <https://doi.org/10.1172/JCI74778>.
57. Manning-Geist, B.L., Sullivan, M.W., Zhou, Q., Iasonos, A., Selenica, P., Stallworth, C., Liu, Y.L., Long Roche, K., Gordhandas, S., Aghajanian, C., et al. (2024). Folate receptor alpha expression in low-grade serous ovarian cancer: Exploring new therapeutic possibilities. *Gynecol. Oncol.* *188*, 52–57. <https://doi.org/10.1016/j.ygyno.2024.06.008>.
58. Moore, K.N., Angelergues, A., Konecny, G.E., Garcia, Y., Banerjee, S., Lorusso, D., Lee, J.Y., Moroney, J.W., Colombo, N., Roszak, A., et al. (2023). Mirvetuximab Soravtansine in FRalpha-Positive, Platinum-Resistant Ovarian Cancer. *N. Engl. J. Med.* *389*, 2162–2174. <https://doi.org/10.1056/NEJMoa2309169>.
59. Perez-Riverol, Y., Bai, J., Bandla, C., Garcia-Seisdedos, D., Hewapathirana, S., Kamatchinathan, S., Kundu, D.J., Prakash, A., Frericks-Zipper, A., Eisenacher, M., et al. (2022). The PRIDE database resources in 2022: a hub for mass spectrometry-based proteomics evidences. *Nucleic Acids Res.* *50*, D543–D552. <https://doi.org/10.1093/nar/gkab1038>.
60. Brunner, A.D., Thielert, M., Vasilopoulou, C., Ammar, C., Coscia, F., Mund, A., Hoerning, O.B., Bache, N., Apalategui, A., Lubeck, M., et al. (2022). Ultra-high sensitivity mass spectrometry quantifies single-cell proteome changes upon perturbation. *Mol. Syst. Biol.* *18*, e10798. <https://doi.org/10.15252/msb.202110798>.
61. Demichev, V., Messner, C.B., Vernardis, S.I., Lilley, K.S., and Ralser, M. (2020). DIA-NN: neural networks and interference correction enable deep proteome coverage in high throughput. *Nat. Methods* *17*, 41–44. <https://doi.org/10.1038/s41592-019-0638-x>.
62. Muller-Reif, J.B., Hansen, F.M., Schweizer, L., Treit, P.V., Geyer, P.E., and Mann, M. (2021). A New Parallel High-Pressure Packing System Enables Rapid Multiplexed Production of Capillary Columns. *Mol. Cell. Proteomics* *20*, 100082. <https://doi.org/10.1016/j.mcpro.2021.100082>.
63. Meier, F., Brunner, A.D., Frank, M., Ha, A., Bludau, I., Voytik, E., Kaspar-Schoenefeld, S., Lubeck, M., Raether, O., Bache, N., et al. (2020). diaPASEF: parallel accumulation-serial fragmentation combined with data-independent acquisition. *Nat. Methods* *17*, 1229–1236. <https://doi.org/10.1038/s41592-020-00998-0>.
64. Demichev, V., Szyrwiel, L., Yu, F., Teo, G.C., Rosenberger, G., Niewianda, A., Ludwig, D., Decker, J., Kaspar-Schoenefeld, S., Lilley, K.S., et al. (2022). dia-PASEF data analysis using FragPipe and DIA-NN for deep proteomics of low sample amounts. *Nat. Commun.* *13*, 3944. <https://doi.org/10.1038/s41467-022-31492-0>.
65. Bredikhin, D., Kats, I., and Stegle, O. (2022). MUON: multimodal omics analysis framework. *Genome Biol.* *23*, 42. <https://doi.org/10.1186/s13059-021-02577-8>.
66. Kadri, S., Long, B.C., Mujacic, I., Zhen, C.J., Wurst, M.N., Sharma, S., McDonald, N., Niu, N., Benhamed, S., Tuteja, J.H., et al. (2017). Clinical Validation of a Next-Generation Sequencing Genomic Oncology Panel via Cross-Platform Benchmarking against Established Amplicon Sequencing Assays. *J. Mol. Diagn.* *19*, 43–56. <https://doi.org/10.1016/j.jmoldx.2016.07.012>.
67. Talevich, E., Shain, A.H., Botton, T., and Bastian, B.C. (2016). CNVkit: Genome-Wide Copy Number Detection and Visualization from Targeted DNA Sequencing. *PLoS Comput. Biol.* *12*, e1004873. <https://doi.org/10.1371/journal.pcbi.1004873>.

STAR★METHODS

KEY RESOURCES TABLE

| REAGENT or RESOURCE | SOURCE | IDENTIFIER |
|--|--|---|
| Antibodies | | |
| Rabbit monoclonal anti-EPCAM | Abcam | Cat# ab275122; RRID: AB_3678774 |
| Rabbit monoclonal anti-Decorin | Abcam | Cat# ab281326; RRID: AB_3678775 |
| Rabbit polyclonal anti-NOVA2 | Novus Biologicals | Cat# NBP1-92196; RRID: AB_11034679 |
| Mouse monoclonal anti-c-MET | Invitrogen | Cat# 18-7366; RRID: AB_2533047 |
| Mouse monoclonal anti-NNMT | Santa Cruz Biotechnology | Cat# sc-376048; RRID: AB_10988227 |
| Mouse monoclonal anti-FOLR1 | Cell Signaling | Cat# 37283S, clone: BN3.2; RRID: AB_3678776 |
| Rabbit polyclonal anti-ITGB1 | Sigma Aldrich | Cat# HPA069003; RRID: AB_2732125 |
| Rabbit polyclonal anti-FN1 | Abcam | Cat# ab2413; RRID: AB_2262874 |
| Mouse monoclonal anti-PAX8 | Cell Signaling Technology | Cat# 28556; RRID: AB_3678777 |
| Rabbit polyclonal anti-CAPS | Thermo Fisher Scientific | Cat# PA5-60401; RRID: AB_2639273 |
| Goat anti-Mouse IgG1 AF647 | Thermo Fisher Scientific | Cat# A-21240; RRID: AB_2535809 |
| Goat anti-rabbit IgG AF750 | Abcam | Cat# ab175735; RRID: AB_3678778 |
| Biological samples | | |
| FFPE tissue specimen of SBT, SBT-MP, LGSC, and LGSC-Met | University of Chicago | Ovarian cancer database |
| Chemicals, peptides, and recombinant proteins | | |
| ConcavalinA conjugated to tetramethylrhodamine | Thermo Fisher Scientific | Cat# C860 |
| SYTOX green | Thermo Fisher Scientific | Cat# S7020 |
| LysC | Wako | Cat# 129-02541 |
| Trypsin | Sigma-Aldrich | Cat# T6567 |
| Proteinase K | Agilent | S3004 |
| Inhibitors for <i>in vitro</i> validation, see Table S3E (Tab 'Inhibitor Testing') | Diverse | N/A |
| Critical commercial assays | | |
| 96-Well Cell Invasion Assay, Collagen I | Cell BioLabs Inc. | CBA-112-COL |
| Deposited data | | |
| Mass spectrometry-based proteomics data | This paper | PRIDE: PXD046354 |
| GeoMx spatial transcriptomics data | This paper | GEO: GSE289044 |
| Experimental models: Cell lines | | |
| VOA3448 | M. Carey, University of British Columbia | CVCL_VQ40 |
| VOA4627 | M. Carey, University of British Columbia | CVCL_VQ38 |
| VOA6406 | M. Carey, University of British Columbia | CVCL_VQ52 |
| MPSC-1 | I-M. Shih, Johns Hopkins University | CVCL_9822 |
| CAISMOV24 | F. Guimarães, University of Campinas, Brazil | CVCL_A5TC |
| CAF 316 | N/A | Patient-derived cell clone |
| Experimental models: Organisms/strains | | |
| Mouse: Female HSD:Athymic Nude-Foxn1nu (athymic nude; #069(nu)/070(nu/+)) | Charles River | N/A |

(Continued on next page)

Continued

| REAGENT or RESOURCE | SOURCE | IDENTIFIER |
|--|---|---|
| Oligonucleotides | | |
| siRNA for <i>in vitro</i> knock-downs, see Table S3D (Tab 'siRNA testing') | Horizon Discovery | N/A |
| NNMT conditioned media: shCtrl, 5'-GCAGTTATCTGGAAGATCAGG-3' | In-house | N/A |
| NNMT conditioned media: shNNMT 5'-GCTACACAATCGAATGGTT-3' | In-house | N/A |
| Software and algorithms | | |
| Biology Image Analysis Software (BIAS) | Mund and Coscia et al. ¹³ | https://single-cell-technologies.com |
| DIA-NN, version 1.8.0 | Demichev et al. ^{60,61} | https://github.com/vdemichev/DiaNN |
| R statistical environment, version 4.2.2 | R Development Core Team | https://www.r-project.org/ |
| CIBERSORTx | Newman et al. ⁴⁴ | https://cibersortx.stanford.edu/ |
| MOFA+ (Multi-Omics Factor Analysis) | Argelaguet et al. ⁴³ | https://biofam.github.io/MOFA2/ |
| GraphPad Prism | Licensed software | https://www.graphpad.com/features |
| Integrated Genomics Viewer | Broad Institute, MIT Harvard, Cambridge, MA | https://igv.org/ |
| Incucyte® Live Cell Analysis System | Sartorius | https://www.sartorius.com/en/products/live-cell-imaging-analysis/live-cell-analysis-instruments/s3-live-cell-analysis-instrument#id-797316 ; RRID:SCR_023147 |
| StepOnePlus Real-Time PCR System | Applied Biosystems | https://www.thermofisher.com/order/catalog/product/4376600 ; RRID:SCR_015805 |

EXPERIMENTAL MODEL AND STUDY PARTICIPANT DETAILS

Patient cohort, ethics and inclusion statement

Patients who underwent primary surgery for a newly diagnosed borderline ovarian cancer or low-grade serous ovarian cancer at the University of Chicago were retrieved from the University of Chicago ovarian cancer database.⁵⁵ All patients gave written informed consent in compliance with the University of Chicago Institutional Review Board-approved protocol and in accordance with the Declaration of Helsinki. All surgeries were performed by board-certified gynecologic oncologists (S.D.Y., E.L.). Factors for the selection of samples included the representative character of the disease, fixation and pre-analytics, and review by three board-certified pathologists who agreed that these samples were the most representative of the disease state (R.M., A.J.B., R.R.L.). The time between surgery and fixation followed the guidelines of the American Pathology Association (standardized fixation—24 h of formalin). In addition, all samples in the discovery cohort came from the same pathology and pool of surgeons, thereby minimizing sample heterogeneity.

The tumor pathology was reviewed and confirmed by three gynecologic pathologists (R.R.L., R.M., A.B.) before inclusion in the study. The discovery cohort was divided into SBT ($n = 4$), SBT-MP ($n = 4$), primary LGSC-PT ($n = 3$), and corresponding omental metastasis (LGSC-Met, $n = 3$) of which the most representative regions of interest (ROIs) were selected for spatial proteomics and transcriptomics (Table S1). From each ROI, epithelial tumor and stromal cells were extracted where possible to yield one (MS/sequencing) sample for molecular analysis. The validation cohort of 22 patients included 31 tumor samples divided into independent SBT ($n = 9$), SBT components associated with LGSC ($n = 6$), LGSC-PT ($n = 7$) and LGSC-Met ($n = 9$). The study followed the Global Code of Conduct for international research.

Mouse models

Animal studies were reviewed and approved by the Institutional Animal Care and Use Committee of the University of Chicago. Female HSD:ATHymic Nude-Foxn1^{nu} (athymic nude; #069(nu)/070(nu/+)) mice at age 5–6 weeks and approximately 20 grams were purchased from Charles River. Mice were irradiated and injected intra-peritoneally (i.p.) with 5 million VOA6406 cells. The mice were sacrificed 12 weeks post cancer cell injection. The omental tumors were collected, minced into 1mm³ pieces, and digested with 2.5U/ml dispase II (17105041, Gibco) at 37°C and 5% CO₂ for 30 min. Single cells were collected by 70 μm filtration, washed twice in PBS, and plated in growth media. After a 30-min incubation, the unadhered cells were collected and plated in a new flask. These mouse tumor derived cells, VOA6406ip1, were passaged 10 times and validated using short tandem repeat DNA fingerprinting with the AmpFSTR Identifier kit and compared with known fingerprints by IDEXX BioAnalytics Laboratories (Columbia, MO).

Cell lines

VOA3448, VOA4627, and VOA6406 (M. Carey, University of British Columbia) cells were cultured in a 1:1 mixture of MCDB 105 (Cell Application Inc.) and Medium 199 (Gibco), supplemented with sodium bicarbonate (Corning), L-glutamine (Corning), and 10% fetal bovine serum (FBS). MPSC-1 (I-M. Shih, Johns Hopkins University) and CAISMOV24 (F. Guimarães, University of Campinas, Brazil) cells were cultured in RPMI-1640 (Cell Application Inc.) supplemented with L-glutamine (2mM) and 10% FBS. The cells were maintained at 37°C in a humidified incubator at 5% CO₂. The cell lines were banked in liquid nitrogen and one vial of each passage was confirmed *Mycoplasma* negative using the STAT-Myco kit. The cell lines were validated using short tandem repeat DNA fingerprinting with the AmpF Φ STR Identifier kit and compared with known fingerprints by IDEXX BioAnalytics Laboratories (Columbia, MO). Cells were passaged 2–10 times after thawing before commencing with experiments.

METHOD DETAILS

Deep Visual Proteomics

Immunofluorescence

Formalin-fixed paraffin-embedded (FFPE) tissue was sectioned (2.5 μ m) from paraffin blocks and mounted on 1.0 PEN membrane slides (MicroDissect, MDG3P40AK). To enhance tissue adhesion, membrane slides were incubated for 1 h under UV light and treated with VECTABOND reagent (Biozol, VEC-SP-1800) according to the manufacturer's instructions. Mounted slides were incubated at 55°C for 30 min and deparaffinized through xylene (2 min) and 100% ethanol, 95% ethanol, 75% ethanol, 30% ethanol, and distilled water (1 min) twice. Antigen retrieval occurred in 1x DAKO pH9 HIER buffer (Agilent Dako)/10% glycerol (v/v) (Sigma) in a preheated water bath at 90°C for 60 min, followed by the blocking of nonspecific binding sites using 5% BSA in PBS for 60 min at room temperature.

Directly conjugated antibodies targeting EPCAM (Abcam, recombinant Alexa Fluor 555, ab275122, 1:100) and decorin (Abcam, recombinant Alexa Fluor 647, ab281326, 1:100) were diluted in antibody diluent solution (Agilent Dako, S080983-2) and incubated at 4°C overnight in a wet staining chamber. Nuclei were stained with SYTOX green (1:400, Thermo Fisher Scientific) for 10 min at room temperature and mounted with aqueous mounting medium (SlowFade Diamond Antifade Mountant, Thermo Fisher Scientific).

Image acquisition and analysis

High-resolution fluorescence images were acquired on an Axio Scan.Z1 (Zeiss) microscope, coupled to a 20x/0.8 M27 dry objective, and the scanned slides were saved as 'czi' files. Images were recorded implementing a 10% tile overlap, five z-stacks (offset -5 μ m) and a bin mode of 1x.1, using optimized exposure times for each fluorescent channel (AF647: 40ms, AF555: 300ms, AF488: 10ms). For image post-processing, z-planes were collapsed into a single plane based on the variance of pixel values ('Extended Depth of Focus - EDF') and stitched to achieve precise matching of tiles. Then, images were imported into the Biology Image Analysis Software ('BIAS') and analyzed.¹³ Briefly, segmentation was performed for epithelial cells (Algorithm: 'Generic cytoplasm segmentation v1.0', Settings: input spatial scaling: 1.0, detection confidence: 50%, contour confidence: 50%, region properties: 10–500 μ m²) and stromal cell equivalents (Algorithm: Generic nucleus segmentation v1.0. Settings: input spatial scaling: 2.4, detection confidence: 50%, contour confidence: 50%, region properties: max. 100 μ m², dilated by 9 μ m²). Of note, stromal cells were acquired using an algorithm dilating the shape of stromal nuclei as approximation.

Once regions of interest were selected using matching regions in spatial transcriptomics, shapes of single cells were exported while defining three reference points for coordinate system transfer. To improve the efficiency of laser-guided shape extraction, polygon reduction was accomplished by implementing the Ramer-Douglas-Peucker algorithm. To facilitate this, an interactive web interface was developed using Python (version 3.8.5) in conjunction with the Streamlit library (version 1.19.0). Internally, data manipulation tasks were carried out using the numpy (version 1.22.2) and pandas (version 1.4.0) libraries. Visualization of both original and reduced shapes was performed using the plotly library (version 5.5.0). Epsilon values were chosen interactively to find an optimum to preserve shapes and reduce points. Upon image acquisition, cover glasses were removed, and the tissue was dried thoroughly at room temperature to enable precise laser cutting.

Laser microdissection

Cells were cut from the tissue using the laser microscope (Leica Microsystems) and collected into a dry 384-well plate (Eppendorf) while maintaining a stable temperature of 31.9°C. AI-defined shapes of cells were imported using the reference points defined in the BIAS software and minimal correction of shape alignment was performed. Laser extraction was performed directing a diode-pumped solid-state laser (349 nm) via an HC PL FLUOTAR L 63x/0.70 objective (power: 59, aperture: 1, speed: 20–25, head current: 42–49%, pulse frequency: 2450–2600, offset: 214–219) conducting a final middle pulse to collect the shapes vertically into the well. Considering the surface area of the cell as an indicator of final protein amounts injected into the mass spectrometer, a total of 700 epithelial cell shapes and 150 stroma equivalents were collected to compensate for differences in area sizes.

Sample preparation

All laser-dissected samples in the 384-well plate were processed in parallel by implementing an automated liquid handling platform (Agilent Bravo). Extracted cells were concentrated at the bottom of each well by the addition of 28 μ L of 100% acetonitrile, centrifugation at 2,000 g for 10 min and vacuum evaporation for 15 min (60°C). Cells were lysed in 4 μ L of 60 mM triethylammonium bicarbonate (TEAB) in H₂O at 95°C for 60 min. After adding 1 μ L of 60% acetonitrile (final concentration of 12% (v/v)), the samples were incubated at 75°C for 60 min. Proteins were digested sequentially, adding 1 μ L of 4ng/ μ L LysC (Wako, 129–02541; in 60 mM TEAB, 12% I) for 3 h and 1.5 μ L of 4 ng/ μ L trypsin (Sigma-Aldrich, T6567; in 60 mM TEAB, 12% I) overnight at 37°C. The enzymatic digest

was quenched using a final concentration of 1% (v/v) trifluoroacetic acid (TFA), centrifuged for 5 min at 1,000g and vacuum dried at 60°C. Samples were resuspended in 2% acetonitrile (v/v), 0.1% trifluoroacetic acid (v/v), and the entire volume was injected for MS data acquisition.

Mass spectrometry measurements and data processing

The LC system of choice was an EASY nanoLC 1200 (Thermo Fisher Scientific). Peptides were separated on a 50 cm in-house packed HPLC column⁶² (75 μ m inner diameter packed with 1.9 μ m ReproSil-Pur C18-AQ silica beads (Dr. Maisch GmbH)) with a linear gradient of 120 min from 3 to 30% buffer B in 95 min, followed by an increase to 60% for 5 min, washed at 95% buffer B for 10 min and re-equilibration for 10 min at 5% buffer B (buffer A: 0.1% formic acid (FA) and 99.9% ddH₂O; buffer B: 0.1% FA, 80% ACN, and 19.9% ddH₂O). The flow rate was kept constant at 300 nL/min, and the column was heated to 60°C by an in-house manufactured oven. The EASY LC system was coupled to a timsTOF SCP mass spectrometer (Bruker) via a nanoelectrospray ion source (Captive spray source, Bruker). The mass spectrometer was operated in dia-PASEF mode using the 16 diaPASEF scan acquisition scheme (standard scheme).⁶³ The method covered an m/z range from 400 to 1200 and ion mobility of 0.6–1.6 Vs. cm⁻². All other settings were described previously.⁶⁰ For cell line experiments, the LC system was coupled to a timsTOF Pro2 mass spectrometer (Bruker) with settings as described above.

Raw data was searched using the DIA-NN software^{61,64} (version 1.8.0). Searches were performed separately for the epithelial and stromal compartments using the library-free search and the human Uniprot databases (UP000005640_9606 with isoforms, February 28, 2022). In short, a deep-learning module, match-between-runs (MBR) and heuristic protein inference ('-relaxed-prot-inf') was enabled. N-terminal methionine excision and carbamidomethylation were set as fixed modifications, 'IDs, RT & IM profiling' was used for library generation, 'robust LC (high accuracy)' for quantification and 'Global' for cross-run normalization. The 'pg_matrix.tsv' output file was used for further data analysis. For quality control only, epithelial and stromal data were jointly quantified in DIA-NN as described above.

Bulk proteomics of cell lines

Cells were harvested and washed in PBS. Pellets were lysed for 10 min at 90°C in 50 μ L lysis buffer (12.5% acetonitrile, 300 mM Tris/HCl pH 8.0, 5 mM TCEP, 25 mM CAA), sonicated in a Bioruptor Plus (Diagenode, sonication cycles of 30 s for 15 min) and heated at 90°C for 30 min. Protein concentration was measured using a Nanodrop instrument (ThermoFisher Scientific), proteins were digested using LysC and trypsin in a ratio of 1:100 over night at 37°C. Digests were quenched by adding trifluoroacetic acid (TFA) to a final concentration of 1%, and peptides purified using two layers of SDB-RPS as active matrix in stage tips (Wash 1: isopropanol, 1% TFA; Wash 2: 0.2% TFA; elution buffer (80% I, 1% NH₄+)). Purified peptides were vacuum dried for 40 min at 60°C and resuspended in 2% acetonitrile (v/v), 0.1% trifluoroacetic acid (v/v). A total of 200ng was injected into the mass spectrometer and measured as described above. For siRNA knock-down experiments for NOVA2, VOA6406 cells were treated with a 25 nM siRNA pool for NOVA2 (L-012590-00, see below). 500,000 cells were harvested, washed in PBS and prepared for MS as described above.

GeoMx spatial transcriptomics

FFPE tissue sections (5 μ m) sliced consecutively to Deep Viusal Proteomics samples were processed following the Nanostring GeoMx user manual (MAN-10132-04). In brief, tissue slides were deparaffinized and rehydrated, followed by protein target retrieval using antigen retrieval buffer (Tris-EDTA) for 20 min in a pressure cooker. RNA target retrieval was accomplished by a digest with proteinase K for 15 min at 37°C. Tissue was post-fixed in 10% NBF, followed by an overnight hybridization at 37°C with the RNA probes (Human Whole Transcriptome Atlas, 18,000 protein-coding genes coupled to UV-cleavable oligonucleotide barcodes). Excess probes were removed the next day by washing the samples twice in stringent washes at 37°C, followed by an incubation period in blocking buffer W (Nanostring LOT#:2-23020032). Thereafter, tissue was stained using conjugated primary antibodies targeting pan-cytokeratin (mouse monoclonal antibody, Novus NBP2-33200AF488, 1:100) and vimentin (mouse monoclonal IgG1 κ , Santa Cruz sc-373717, 1:100) as well as the SYTO13 nuclear stain (ThermoFisher Scientific, S7575) for one hour at room temperature.

For transcriptomics data acquisition, slides were placed on the GeoMx Digital Spatial Profiler (DSP) and scanned in 20 \times magnification. Based on immunofluorescence images, regions of interest (ROIs) were collected under supervision of an experienced pathologist (AB) and matched to the regions selected in DVP. Upon ROI selection, oligonucleotide barcodes were collected into a 96-well plate by UV-ablation while precisely separating compartments in each region. Sequencing libraries were prepared using the Illumina TruSeq technology for the ligation of sequencing adaptors and amplification. Amplified libraries were purified using two rounds of Ampure XP magnetic bead cleanup (ratio 1.2:1 (beads: library)) (HighPrep PCR from MAGBIO (Cat#: AC-60500)). Purified libraries were sequenced in an Illumina NovaSeq flowcell PE50 at a depth of 100 \times μ m².

Advanced data integration

Multimodal analysis was conducted using the MOFA+ (Multi-Omics Factor Analysis)⁴³ platform to integrate the Nanostring and DVP datasets. For this analysis, we only included transcripts and proteins previously identified as differentially expressed (1385 genes and 962 proteins for epithelium; 1013 genes and 628 proteins for stroma). Samples with multiple measurements were mean-aggregated, leading to 140 Nanostring and 42 DVP samples (from 143 samples combined) for epithelium and 102 Nanostring and 37 DVP samples (from 111 samples combined) for stroma. We applied separately for each cell type (epithelium and stroma) using muon, a dedicated Python framework for multimodal omics analysis.^{43,65} The analysis was performed on the union of Nanostring and DVP samples, and four latent factors were learned for each tissue type. For the integrated marker panel, transcripts and proteins were sorted by MOFA

score and the top10 ranks for each modality and enrichment (drivers of SBT and LGSC, respectively) were selected for tumor and stromal cells.

Antibody-based validation staining

Immunohistochemistry

FFPE tissue was sectioned (5 μ m) on SuperfrostTM Plus Microscope Slides (Fisher Scientific, 22-037-246). Then, the immunohistochemistry was performed on Leica Bond RX automated stainer. After the standard procedures for deparaffinization and rehydration, tissue sections were treated with Proteinase K (Agilent, S3004) for 5 min pre-treatment at room temperature. Anti-NOVA2 [Novus Biologicals, # NBP1-92196, 1:50], c-MET [Invitrogen, #18-7366, 1:150], NNMT [Santa Cruz Biotechnology, #sc-376048, 1:100], FOLR1 [Cell Signaling, 37283S, clone: BN3.2, 1:50], ITGB1 [Sigma Aldrich, HPA069003-100UL, 1:100], FN1 [Abcam, ab2413, 1:200] was applied on tissue sections for 60 min incubation at room temperature. The antigen-antibody binding was detected by Bond Polymer Refine Detection (DS9800, Leica Microsystem). Tissue sections were briefly immersed in hematoxylin for counterstaining and were covered with cover glasses. These slides were imaged using Olympus VS200 Slideview. Images for publication were exported from QuPath version 0.3.2.

Immunofluorescence

FFPE tissue was sectioned (5 μ m) on SuperfrostTM Plus Microscope Slides (Fisher Scientific, 22-037-246) and deparaffinized as described above (see section 'Deep Visual Proteomics'). For antigen-retrieval, samples were heated in a water bath at 90°C for 30 min in 1x DAKO pH9 HIER buffer (Agilent Dako) and blocked using 5% BSA in PBS for 45 min at room temperature. Primary antibodies for PAX8 (Mouse mAb 28556, Cell Signaling Technology, 1:400) and CAPS (Rabbit polyclonal PA5-60401, Thermo Fisher Scientific, 1:50) were diluted in antibody diluent solution (Agilent Dako, S080983-2) and incubated at 4°C overnight in a wet staining chamber. Secondary antibodies (anti-Mouse IgG1 AF647, A-21240, Thermo Fisher Scientific, 1:200; anti-rabbit IgG AF750, ab175735, Abcam, 1:200) and ConcanavalinA conjugated to tetramethylrhodamine (C860, Thermo Fisher Scientific, 1:150) were incubated for 60 min at room temperature. Nuclear staining was performed using SYTOX green (1:400, Thermo Fisher Scientific) for 10 min at room temperature and slides were mounted (Vectashield Vibrance Antifade Mounting Medium, Vector Laboratories, H-1700). The resulting staining was visualized on a Axio Scan.Z1 (Zeiss) microscope as described above (see section 'Deep Visual Proteomics').

siRNA transfection

We used the integrated panel presented in [Table S3C](#) as a starting point for the selection of siRNA screen targets. We complemented these targets with proteins/transcripts from the differential expression ([Tables S2E](#), [S2I](#), [S4C](#), and [S4F](#)) and regression ([Tables S2D](#) and [S4D](#)) analyses which we screened using current scientific literature for biological significance in cancer. For transient transfections, LGSC were transfected with 25 nM small interfering siRNA pools using DharmaFECT 1 (Horizon Discovery) in M105:M199 media without FBS. Each pool contained four siRNA sequences for 23 proteins ([Table S3D](#)) as well as controls, ON-TARGET plus Non-targeting siRNA #1 (D-001810-01), or siGLO RISC-Free Control reagent (Horizon Discovery; Catalog number; D-001600-01-05).

Inhibitor testing

The MET inhibitors, Savolitinib (HY-15959) and Cabozantinib (YT-13016), the EGFR inhibitors, Icotinib (HY-15164A), Lapatinib (HY-50898) and Erlotinib (HY-50896), MEK1/2 inhibitor Trametinib (HY-10999), BRAF inhibitor Dabrafenib (HY-14660), and the integrin alpha 5 antibody (IIA1) were purchased from MedChem Express. The FOLR1-targeted antibody drug conjugate, Mirvetuximab was purchased from ImmunoGen, Inc. The CDK inhibitors, Abemaciclib (LY2835219), Milciclib (PHA-848125), and Palbociclib (S4482), the MMP2/9 inhibitor SB-3CT (S7430), c-Fos AP-1 inhibitor T-5224 (S8966), JAK 1/2 inhibitor Rrxolitinib (S1378), and the TGF β R1 inhibitor galunisertib (LY2157299) were purchased from SelleckChem. The inhibitors were tested *in vitro* using the proliferation IC50 doses ([Table S3E](#)). IC50 values of set I compounds were determined using an MTT assay evaluation proliferation on the epithelial cancer cells only. For set II compounds, the IC50 was determined from the mean results derived from epithelial cancer cells alone and in co-culture with CAFs to accommodate cancer-cell and co-culture experimental conditions.

Quantitative PCR with reverse transcription

RT-qPCR was conducted by StepOnePlus Real-Time PCR System (Applied Biosystems). Total RNA was extracted using TRIzol (Invitrogen) and transcribed into cDNA using TaqMan RNA Reverse Transcription Kit (Applied Biosystems). A TaqMan endogenous control was used to normalize mRNA expression. Each PCR assay was performed in triplicate, and relative levels of NOVA2 expression were calculated using the $2^{-\Delta\Delta C_t}$ method.

Genomic sequencing

Next-generation sequencing (NGS) was performed using the University of Chicago Medicine OncoPlus (UCM-OncoPlus) panel, a hybrid-capture panel targeting 1005 cancer-associated genes with 168 clinically reported genes. DNA extraction, DNA quantification, library preparation, and NGS were performed as described previously.⁶⁶ Data analysis was performed on a high-performance computing system (Center for Research Informatics, University of Chicago) using an in-house developed bioinformatics pipeline. Variant review and classification included filters based on population variant frequencies (The 1000 Genomes Project, <https://www.internationalgenome.org/>), variant frequencies in cancer databases (COSMIC: catalog of somatic mutations in cancer, <https://cancer.sanger.ac.uk/cosmic> and cBioPortal, <https://www.cbioportal.org/>), and coding effects. Somatic variant calls were

inspected using Integrated Genomics Viewer (IGV; Broad Institute, MIT Harvard, Cambridge, MA). Copy number results were calculated using a combination of CNVkit⁶⁷ software and additional in-house intra-run normalization to eliminate run-specific artifacts by comparison with a pooled cohort of clinical controls. Gene-level changes were called using the UCM-OncoPlus clinical interpretation criteria as previously described.⁶⁶

Functional assays

Migration/siRNA screen

Ovarian cancer cells were plated in 96-well plates (17,000 cells/well) and reverse transfected with target or control siRNA. The wells were washed thoroughly with phosphate buffered saline (PBS) to remove detached cells and growth media added to each well before scratching with a wound making machine. The cells were monitored on the IncuCyte Live Cell Analysis System (Sartorius), with the wells imaged every hour to evaluate migration.

Proliferation

Ovarian cancer cells were plated onto 96-well plates (2–4,000 cells/well) and incubated for 24 h to allow cells to adhere before media changed. For siRNA testing, the cells were pre-transfected with target or control siRNA 24 h prior to assay and treated with growth media. For inhibitor testing, the cells were treated with IC50 concentration of inhibitors in growth media (Table S3E). For conditioned media testing, 24 h conditioned media was collected from primary human CAFs that stably expressed non-targeting shCtrl (5'-GCAGTTATCTGGAAGATCAGG-3') or shNNMT (5'-GCTACACAATCGAATGGTT-3'). The LGSC cells were treated, incubated at 37°C with 5% CO₂, and monitored on the IncuCyte Live Cell Analysis System (Sartorius), with the wells imaged every 4–12 h to evaluate proliferation.

Invasion

Ovarian cancer cells were plated in the top well of the 24-well Boyden chamber coated with 6 μg of rat tail collagen type I (200,000 LGSC cells/well; Figures 6D and 7C left, S14D, S14H left) or ovarian cancer cells were plated in the top well of the QCMTM 96-Well Cell Invasion Assay plate (40,000 LGSC cells and 4,000 CAFs/well; Figures 6G and 7C right, 7D, S14F, S14H right, S14J). For siRNA testing, the cells were pre-transfected with target or control siRNA 24 h prior to assay in serum-free media. For inhibitor testing, the cells were treated with IC50 concentration of inhibitors in serum-free media (Table S3E). Growth media was placed in the bottom chamber for the siRNA and inhibitor testing. For CAF conditioned media testing, conditioned media was collected from primary human CAFs that stably expressed shCtrl or shNNMT as described above. The LGSC cells were plated in serum-free media, and in the bottom chamber CAF control media, shCtrl-expressing CAF conditioned media, or shNNMT-expressing CAF conditioned media, was added. The cells were incubated for 48 h to allow the cells to invade through the chamber. For the 24-well Boyden chamber, the invaded cells were stained with crystal violet, imaged (Nikon Ti2 Eclipse fully automated inverted fluorescence microscope), and counted using ImageJ Cell Counter plugin. For the QCMTM 96-Well Cell Invasion Assay, the invaded cells were detached, lysed, and stained with CyQuant GR Dye according to manufacturer instructions. Total fluorescence (480/520 nm) was acquired on a fluorescent plate reader (SpectraMax iD5).

In vivo compound intervention

One million VOA6406ip1 cells were injected intraperitoneal (i.p.) in 7-week-old athymic nude mice (day 1). Treatment was initiated on day 14 with a one-time intravenous treatment of mirvetuximab soravtansine (2.5 mg/kg) or PBS control 10 μL, followed by i.p. treatment of Milciclib (40 mg/kg) or DMSO control in 200 μL PBS on days 15–20 and days 22–27. On day 28, total tumor number, total tumor weight and total ascites volume of each mouse was measured.

QUANTIFICATION AND STATISTICAL ANALYSIS

Bioinformatics analyses of Deep Visual Proteomics and spatial transcriptomics data were performed in the R statistical environment (version 4.2.2). Protein intensities and GeoMx counts were log₂ transformed and evaluated as described below. For each dataset, samples belonging to the main cohort were selected, while addition samples ('case studies') were processed separately. For proteomic quality control, data completeness was determined by calculating the number of regions (0–3) where a protein was consistently identified across a specimen. Coefficients of variations (CVs) were determined on non-logarithmic data and complete MS intensities (no 'NA' values) (i) within a specimen (intra-specimen) by calculating the variation between different regions and the mean CV values for each group and (ii) between specimen (inter-specimen) by calculating mean MS intensities of regions for each specimen and the CVs of mean region values within each cohort group.

GeoMx raw count data was processed and normalized using the R GeoMxTools package. Segments with fewer than 1000 raw reads, below ~75% for % Aligned, ~80% for % Trimmed and Stitched sequencing reads, were removed. We also removed segments with sequencing saturation <50%, negative count <1, and No Template Control count >9000. A probe is removed globally if the geometric mean of that probe's counts from all segments divided by the geometric mean of all probe counts representing the target from all segments is less than 0.1 or the probe is an outlier according to the Grubb's test in at least 20% of the segments. Segments with less than 5% of the genes detected were removed, and genes detected in at least 5% of the segments were kept. Counts were then normalized by Q3 normalization.

Differential protein/transcript abundances of both datasets were determined using the 'Limma' package (v3.54.2) using the false discovery rate (FDR) for multiple testing correction and fixed parameters (adjusted *p*-value ≤ 0.05 and logarithmic foldchange >1.5) for the assessment of significance. Likewise, 'Limma' was used for regression analyses across groups using a linear model fit

followed by empirical Bayes statistics, while the same significance cutoff was used as described above. An overlap of MS protein identification was determined counting 'NA' and valid values per group and a combination matrix for upset plots, as well as all heatmaps, were generated using the ComplexHeatmap package (v2.14.0). For all Principal Component Analyses (PCA) and omics data integration, data were filtered per protein for valid values in 2 out of 3 regions in all specimens of at least one group. Imputed sample from normal distribution (*width of 0.3, downshift of 1.8*). PCA were performed using the FactoMineR package (v2.8). Biological pathway enrichments were accomplished by a gene set enrichment analysis (GSEA) on significantly differentially regulated proteins/transcripts using the WebGestalt gene set analysis toolkit (v0.4.5) in reference to the 'Reactome Pathway' and 'non-redundant geneontology Biological Process' databases and a Benjamini-Hochberg FDR correction (cutoff: 0.05). Ciliated and secretory cell markers were extracted from the top 100 abundant transcripts of the ciliated and secretory cells in the post-menopausal fallopian tube as presented in recently published work.⁴⁵ Remaining plots were generated using the ggplot2 package (v3.4.2) and mean comparisons of *p*-values were added using two-sided Student's *t*-tests and equal variances.

For the integration of omics data, regions of interest were filtered for dataset counterparts and protein/transcript names were matched by first prioritizing non-isoform proteins and then prioritizing the percentage of valid (not 'NA') values when selecting between isoforms. If two ROIs of the spatial transcriptomics matched one DVP region, mean GeoMx counts were calculated. Previously imputed data were used for the proteomic dataset. Correlation between datasets was tested by Pearson correlation using the 'stats' package (v4.2.2) and Benjamini-Hochberg (FDR) correction. Stacked image creation of our multi-omics approach was done with a custom Python script (version 3.10.11) and Adobe Illustrator (27.5) using the following libraries: pandas (1.5.3), untangle (1.2.1), numpy (1.24.3), PIL (9.4.0) and matplotlib (3.7.1). Initially, the shape data was superimposed on raw slide images, followed by manual adjustments as necessary. Subsequently, each color layer was exported separately as an overlay and integrated into Adobe Illustrator. Schematics were created with [BioRender.com](https://www.biorender.com) (Figures 1, 6 and 7) and Adobe Illustrator (Graphical Abstract).

The CIBERSORTx platform⁴⁴ was utilized for digital cell deconvolution of stroma cells from DVP or spatial transcriptomics. The reference file for deconvolution was derived from single-cell RNA sequencing data of the post-menopausal ovary and fallopian tube, with cell types identified from a published manuscript.⁴⁵ Transcripts pre-filtered in this study were processed into a signature matrix using the platform's online interface with standard settings. DVP or spatial transcriptomics stroma files were imported as mixture files and deconvoluted based on the reference data. The resulting cell-type proportions were visualized using the ggplot2 R package (v3.4.2). Cell-adhesion analyses were performed based on the *OmniPath* database³⁰ (intercell network) filtering ligand-receptor proteins by the term 'adhesion' in the categories of intercell-source and target, followed by filtering for significant differential protein regulation comparing SBT vs. LGSC. Chord diagrams were generated using the 'circlize' R package (v.0.4.16). GraphPad Prism was used to evaluate experimental data, including statistical testing as indicated in each figure legend, and data visualization.